Evaluation of Strawberry Quality using Near-Infrared Hyperspectral Imaging (NIR-HSI)

近赤外ハイパースペクトラルイメージングによるイチゴの品質評価

名古屋大学大学院生命農学研究科

森林・環境資源科学専攻

生物システム工学研究分野

関　隼人

２０２３年７月

Contents

1. Introduction

The importance of assessing the quality of agricultural products, although it may vary depending on perspective, is universally accepted as a fundamental requirement. For producers, quality evaluation serves as a crucial tool to affirm the worth and safety of their products, thereby guiding pricing strategies. Superior perceived quality can justify higher pricing, subsequently leading to enhanced profit margins. For sellers, quality assessment forms an integral part of the product selection process. Items distinguished by their high quality ratings tend to attract consumer confidence, potentially boosting sales. Further, demonstrating superior value through quality assessment is a requisite for gauging market expansion in international territories. For consumers, quality ratings provide vital guidelines for making purchasing decisions. With the evolution of food culture, the focus of consumers has shifted from "quantity" to "quality". These ratings thus become key indicators for individuals seeking food options that are safe, tasty, full-flavored, and nutritious. Lastly, quality assessments play a vital role in research by informing researchers and developers about areas of potential enhancement in breeding, cultivation, and distribution techniques.

Quality assessment methodologies are principally bifurcated into two distinct categories: sensory evaluation, utilizing human faculties such as sight, hearing, taste, smell, and touch, and instrument-based analytical evaluation, which aspires to supersede human sensory perception. Notably, these methods are primarily destructive, inducing damage to the samples under examination. Quality is not a uniform attribute in agricultural commodities but varies across different products and even within individual items. A non-destructive evaluation approach is paramount, comprehensively accounting for the distribution of quality within and across personal items to ensure a more precise and accurate quality assessment.

Near-infrared spectroscopy (NIR) serves as a non-destructive evaluation tool for agricultural commodities, operating through the irradiation of near-infrared light (750-2500nm) on a sample and analyzing the transmitted and reflected light spectroscopically. The primary NIR absorption characteristics of molecular vibrations such as O-H, CH, and NH bonds. However, these absorption bands frequently overlap, necessitating the creation of a calibration model via analytical methodologies like chemometrics. The NIR spectra can be influenced by the sample's physical properties and extraneous disturbances, further compounded by the overlapping absorption peaks. Consequently, spectral preprocessing is integral to accurately extracting pertinent information,

employing techniques such as smoothing, baseline correction, and differential processing. The selection of the appropriate method hinges on the specific objectives and the spectral characteristics. The creation of calibration models is paramount to estimating objective variables like sugar content and acidity. This is achieved by employing the pretreated spectral data as explanatory variables, with the models typically falling under the categories of multiple regression models, principal component regression models, or PLS regression models. (Andersson, 2009). In this study, PLS regression is the primary analytical tool, utilizing the principal component (PC) score to maximize covariance between the spectra and the objective variables. This scoring method enhances predictive accuracy. Further, applying PLS in combination with extensive variable selection is employed (H.-D. Li et al., 2018). During the calibration model's formation, data is segmented into training and testing sets. The optimal number of principal components for the PLS is ascertained via cross-validation, which involves additional segmentation of the training data and iterative model construction. Subsequently, the model's efficacy is gauged by fitting it to the test set. The coefficient of determination (R^2), and standard error of prediction (RMSE) serve as evaluative metrics for the model. A model with the marginal deviation between training and testing set results, a coefficient of determination nearing 1, and minimal standard error of prediction is deemed robust. This procedure culminates in the formation of a NIR calibration model. 'Point' Vis-NIR technology, including NIR spectroscopy of fruit, is an established method for estimating harvest time and assessing internal quality attributes (Magwaza et al., 2012; Walsh et al., 2020). Nonetheless, in agricultural commodities, intra-sample spatial variability (for instance, within an individual fruit) necessitates consideration. Point spectroscopy measurements, while taken at various locations on the fruit, represent it entirely, underlining the need for careful intra-sample variability consideration.

Contrary to NIR's point-specific measurement approach, Near-Infrared Hyperspectral Imaging (NIR-HSI) employs a surface-based method that considers spatial distribution. NIR-HSI, a rapidly advancing technique, is extensively utilized for nondestructive assessments of fruit and vegetable quality (Xiaona et al., 2018). A standard hyperspectral imaging system comprises a broadband light source, a hyperspectral camera (encompassing a camera, lens, spectrometer, and area detector), a transport stage, a computer, and software. This system is often referred to as a line-scan type, push-bloom type, among other terminologies. Recently, snapshot-type hyperspectral cameras that internally shift filters for spectroscopy have been introduced. Line scanning

necessitates measurement concurrent with object movement, thus being compatible with a conveyor for real-time inspection. Conversely, the snapshot type does not require object mobility but is unsuitable for imaging in motion due to its method of superimposing two-dimensional images at variant wavelengths using a filter. Primarily, measurements are conducted in reflection mode, favored for its straightforward setup. Data garnered by the NIR-HSI system encompasses spectral information for each pixel within a 2D data matrix, subsequently creating a 3D data amalgamation of spatial and spectral data, designated as a hypercube. These hypercubes incorporate one spectral and two spatial dimensions (Pathmanaban et al., 2019). Preceding research in the domain of NIR-HSI application to agricultural products evidences successful evaluation of parameters such as solid soluble content (SSC) in apples (Ma et al., 2018; Mo et al., 2017) and bananas (Pu et al., 2018), SSC and pH in cherries(X. Li et al., 2018), SSC and hardness in melons (Sun et al., 2017; Tsuta et al., 2002), and SSC, hardness, and pH in kiwifruit(Zhu et al., 2017). Notwithstanding the diverse agricultural products and quality parameters assessed using NIR-HSI, most evaluations predominantly target fruit cross-sections, attributable to the sensitivity of measured hyperspectral data to shape.

Strawberries (Fragaria × ananassa), produced globally, come in diverse varieties due to advanced breeding techniques in Japan. Some of these varieties even boast white flesh. Evaluations of strawberries' value and quality typically hinge on characteristics like color, size, shape, condition, and flavor. However, these assessments are often manually conducted, leading to inconsistencies due to personal bias (Shrestha et al., 2001). Given the rising concerns regarding food quality and safety based on national and international standards, the exploration of automatic technologies to assess fresh strawberries' quality has gained momentum (ElMasry et al., 2007). The organoleptic quality of strawberries is predominantly influenced by sensory attributes such as sweetness and aroma (Darbellay et al., 2002). As strawberries ripen, their sugar content increases, acidity decreases, and their aromatic quality enhances (Sturm et al., 2003). While the color red serves as an essential evaluation criterion for determining ripeness in red strawberries, it poses a challenge for visually assessing the ripeness of white strawberries due to the absence of color variation with ripeness (Tsurumi et al., 2020). The advent of various strawberry varieties necessitates an automated sorting technology for both red-skinned and white-skinned strawberries. The sugar content and sweetness of strawberries can be assessed using sensory evaluation, hydrometers, refractometers, high-pressure liquid chromatography (HPLC), electronic tongues, colorimetric

methods, among others (Magwaza and Opara, 2015). Non-destructive NIR spectroscopy, a field-friendly alternative to these destructive methods, has found applications in evaluating strawberries' internal quality (Sánchez et al., 2012; Włodarska et al., 2019). NIR spectroscopy enables rapid and simple collection of fruits' spectral information, albeit providing only averaged spectra without information about the spatial distribution. Spatial NIR, NIR-HSI, has been utilized to determine the external and internal quality of red strawberries, including ripeness, physical damage, fungal infections, anthocyanins, vitamin C, SSC, and pH content (ElMasry et al., 2007; Liu et al., 2019, 2018; Siedliska et al., 2018; Weng et al., 2020b, 2020a; zhang et al., 2016). However, to the best of our knowledge, no existing works have employed HSI to predict the quality of white strawberries. Earlier studies that employed NIR-HSI gathered spatial-spectral information, utilizing the whole fruit as the region of interest (ROI) to extract an average spectrum. This spectrum was then used to construct a model for estimating the desired quality parameters. Notably, strawberries exhibit an uneven surface with flesh and achenes, and the average spectrum extracted from ROIs does not distinguish between these components with differing characteristics. Moreover, the reflected light from strawberries measured with the NIR-HSI system presented a variable spectrum depending on the shape, an aspect not considered in previous studies. Despite NIR-HSI's ability to capture spatial information, previous studies on strawberries have not fully utilized the information of each pixel.

This paper aims to tackle these issues in strawberry quality evaluation and introduce a novel assessment methodology. We have conducted three studies for this purpose:The purpose of this paper is to overcome the problems in strawberries and to establish a new quality evaluation method, The following three studies were undertaken.

- Visualization of sugar content distribution in white strawberry flesh by NIR-HIS
- 3D imaging of strawberry sugar content by NIR-HSI and shape measurement
- 3D model of strawberry sugar content by Rotation-NIR-HSI

2. Visualization of sugar content distribution of white Strawberry by Near-Infrared hyperspectral imaging

2.1. Introduction

Strawberries with white skin (white strawberries) have recently been introduced in the Japanese market. The accumulation of Anthocyanins (pelargonidin 3-glucoside, pelar-gonidin 3-rutinoside, and cyanidin 3-glucoside), which are the typical red pigments in strawberries (da Silva et al., 2007), is suppressed in white strawberries (Tsurumi et al., 2020; Lin et al., 2018; Salvatierra et al., 2013; Muñoz et al., 2010). Since it is difficult to evaluate the ripeness of white strawberries visually, the development of non-destructive judgment technology is required. However, to our knowledge, no prior works have reported using HSI to predict the quality of white strawberries. In this study, HSI in the range of shortwave infrared (SWIR) wavelengths (900–2500 nm) was used because molecular vibration information is needed to evaluate white strawberries (Golic et al., 2003). The region-of-interest (ROI) used in these studies include pixels corresponding to the flesh (in terms of plant morphology, the accessory fruit, which has an enlarged receptacle) and achene (similar to seeds on the surface, in plant morphology, this is called a true fruit). Major soluble sugars in strawberries, including sucrose, glucose, and fructose, contain in the receptacle. However, these sugars do not contain much in the development of achenes(Fait et al., 2008). However, in earlier works on the visualization of strawberry quality using HSI(Weng et al., 2020b; Fait et al., 2008), the average spectrum calculated from the spectra of all pixels on the fruit surface, including the flesh and achene, was employed to construct regression or discriminant models. The spectrum of each pixel was used to predict the chemical, physical, or category information of a pixel using the developed model. In this present study, first, a method to automatically classify flesh and achene based on the first principal component (PC1) score from the principal component analysis of the surface data of each fruit was developed. Image masks showing pixels of the flesh and the achene were created, the spectra of the whole fruit, flesh, and achene were extracted, and the average spectrum of each was calculated. In this study, using the NIR hyperspectral imaging system, a combination of image processing and chemometric methods for spectra was designed for non-contact Brix evaluation in white strawberries. To achieve these goals, (1) a practical and effective method that automatically extracts information on pixels showing the flesh of fruit samples by

principal component analysis (PCA) imaging and binarization after appropriate pre-processing was developed; this method does not require any training data and, therefore, does not must be developed to evaluate the quality of white strawberries without destroying the sample forecast the degrees Brix of the flesh of fruit using partial least squares regression (PLSR); (3) the developed model for estimating the sugar content of strawberry flesh was applied to pixels showing flesh on the surface of strawberry fruit, and the estimated sugar content for each pixel was obtained. The proposed evaluation method for white strawberries includes a heatmap of the sugar content estimated for each pixel and a violin plot indicating the sugar content distribution for the whole flesh and displaying the flesh's top and bottom.

2.2. Materials and Methods

2.2.1. White strawberry samples

Strawberry samples of the cultivars “Tochigi iW1 go” with white skin were obtained from the Strawberry Research Institute–Tochigi Prefectural Agricultural Experiment Station (Tochigi-Shi, Tochigi Pref. 328-0007, Japan) between February and March 2021. The ripeness and shape varied among the 180 strawberries. Samples were transported by refrigerated shipping after harvest and stored in a standard refrigerator. Before the experiment, the strawberries were kept under controlled conditions at 23 °C for approximately 1 h to reduce variations in measurement caused by temperature changes. Per estimates, 1–2 d had elapsed between harvest and measurement. No serious deterioration in quality was observed visually during the experiment.

2.2.2. NIR Hyperspectral Images and Brix Measurements

Figure. 2-1 shows an overview of the NIR hyperspectral imaging measurement (push-broom line scanning system: Compovision, Sumitomo Electric Industries, Ltd., Tokyo, Japan) and the Brix measurement methods employed in this study. At a spectral interval of 6.2 nm, the camera was equipped with a spectroscope and a 2D photosensitive element (256 pixels (wavelength) × 320 pixels (position)) capable of receiving NIR light from 913 to 2519 nm. A wavelength ranging from 913 to 2166 nm (i.e., 200 wavelength bands) was selected here in because reflectance over 2166 nm has a low signal-to-noise (S/N) ratio. To attain a horizontal field of view of 50 mm for the strawberry samples, the distance between the target and the camera was adjusted with a spatial resolution of 156 μm/pixel. The light source was tube-shaped and illuminated from both sides

using four halogen lamps. The irradiation angle was adjusted to 45°. Each sample was placed on a slider and scanned linewise. The frame rate was set to 30 frames s^{-1}. Both sides were measured by flipping each sample 180°. A soft resin tray was placed between the slider and the sample to hold the sample in place. As a reference, a white plate was measured at 200 frames s^{-1}, and dark images were measured by turning off the light source and covering the lens with a cap. The collected spectral images were converted to relative reflectance values for further analysis using Equation (1), as given below.

$$R_{\lambda,n} = \left(S_{\lambda,n} - D_{\lambda,n}\right)/\left(W_{\lambda,n} - D_{\lambda,n}\right) \quad (1)$$

where λ and n represent the wavelength and pixel index variables, respectively; R_(λ,n) represents the standardized reflectance intensity at wavelength λ and pixel n; S and W represent sample and white reference images, respectively; and D represents dark images. After measuring the hyperspectral data, each measurement surface was divided into two areas indicating the apex and base of the fruit. The fruit sections were then wrapped in a nonwoven cloth, squeezed by hand, and pressed. The juice was stirred well, and the Brix value was measured using a Brix meter (PAL-1, ATAGO Co., Ltd., Tokyo, Japan).

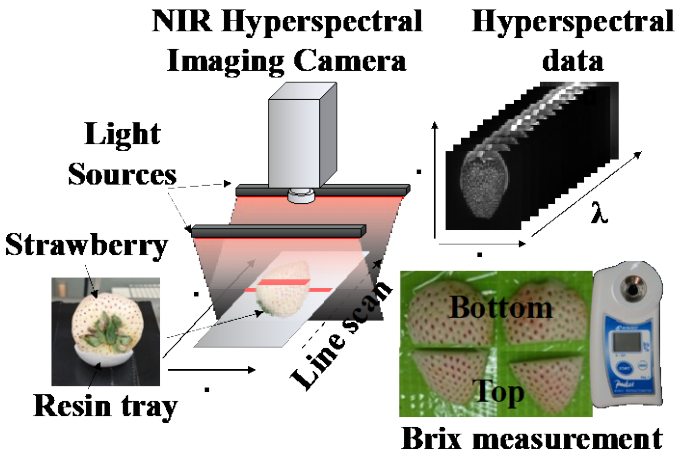

Figure 2-1. This work used the near-infrared hyperspectral imaging (NIR-HSI) system and Brix.

2.2.3. Preprocessing of Hyperspectral Images

The ROI should be predetermined to extract spectral information of strawberries from hyperspectral images. This study determined the ROI of the whole fruit, flesh, and achene in strawberries. The ROI for each part was determined based on PCA and image processing.

2.2.3.1. Creating a fruit mask using thresholding

Figure. 2-2 shows the method used to determine the ROI of the fruit. First, the pixels corresponding to the background, resin tray, and sepals were determined based on the reflectance value at a specific wavelength using thresholding, as shown in Figure 2-2. To determine the wavelength and threshold value for the recognition of the background, resin tray, and sepals, 20 pixels corresponding to the background, resin tray, sepals, and flesh achene, were manually selected. The average and standard deviation spectra of these 20 pixels were calculated, as shown in Figure 2 (right top).

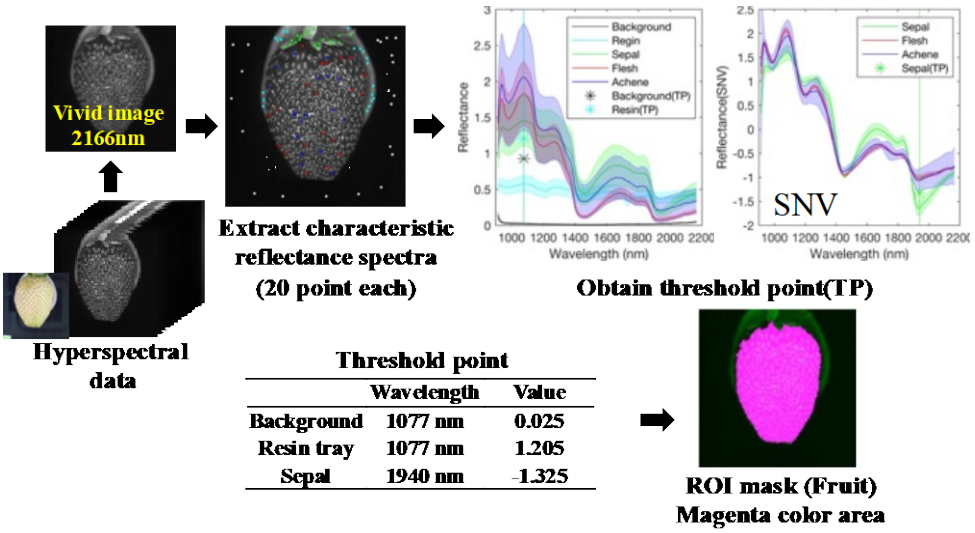

Figure 2-2. Preprocessing procedure for hyperspectral data with ROI extraction by thresholding (Fruit mask).

As the reflectance values at 1077 nm for sepals, flesh, and achene differed significantly from those of the resin tray and background, the reflectance value at 1077 nm was used for the separation of the resin tray and background with a threshold value of 1.205, which is the midpoint of the resin tray and flesh at 1077 nm. After removing the pixels corresponding to the resin tray and background, smoothing with the Savitzky–Golay filter (window size, 7) and standard normal variation (SNV) were conducted for the spectra at each pixel. SNV spectral preprocessing was performed on each pixel to eliminate the physical light-scattering effects and increase the spectral information(Kobori et al., 2013).

$$x_{i,snv} = (x_i - \bar{x})/\left(\sqrt{\sum_{i=1}^{n}(x_i - \bar{x})/(n-1)}\right) \quad (1\text{-}2)$$

where $x_{i,snv}$ denotes the NIR spectrum matrix after SNV pretreatment for the original spectrum x_i, and $\bar{x}$ represents the mean intensity of all wavelengths of the same spectrum. After SNV pretreatment, a significant difference was observed between the sepal part and the flesh or achene part at 1940 nm. Thus, the reflectance value after SNV at 1940 nm was used to determine the pixel corresponding to the sepal with a threshold value of −1.325, which was chosen as the midpoint value of the spectra of the sepal and flesh. Pixels with reflectance greater than 1.205 at 1077 nm and greater than −1.325 after pretreatment at 1940 nm were designated as fruit ROI (including flesh and achene).

2.2.3.2. Determination of ROI corresponding to the flesh part and achene part using combination of PCA and Image processing

Figure. 2-3 depicts the proposed imaging procedure, which combines PCA and image processing to classify pixels corresponding to the flesh parts of strawberries and achenes. This process yielded the ROI corresponding to flesh and achene for the top and bottom of the fruit, which allowed us to calculate the average spectrum from the flesh and achene parts. The raw spectra of the fruit surface were extracted using an ROI mask of only the fruit surface created by a thresholding process. PCA obtained PC1 loading for the spectra after smoothing using a Savitzky–Golay filter and SNV treatment. Autoscaling was performed prior to the PCA. PC1 loading was applied to the hyperspectral data to produce a PC1 image. ROI masks were determined to classify flesh and achene pixels for each sample from the PC1 image binarized using Otsu's method(Otsu, 1979). Moreover, image processing was employed to determine the midpoint coordinates for dividing the fruit into the top and bottom of the fruit mask. Finally, six ROI masks (Fruit-bottom, Fruit-top, Flesh-bottom, Flesh-top, Achene-bottom, and Achene-top) were constructed from each sample, and the average spectrum of each region was computed.

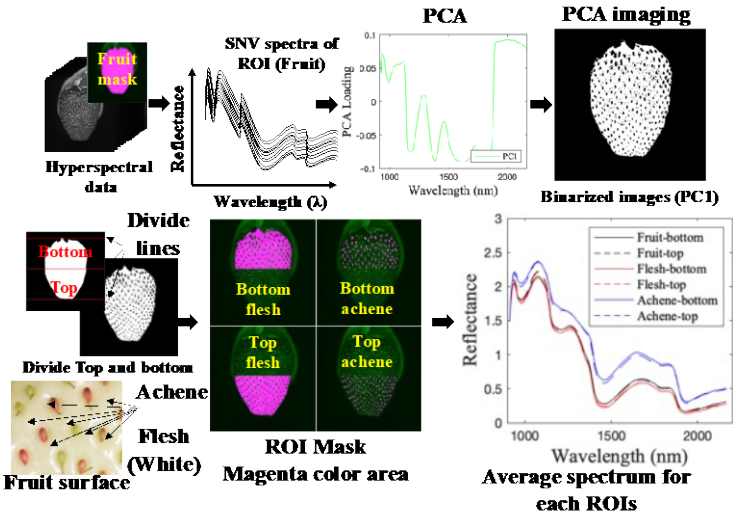

Figure 2-3. Preprocessing procedures for hyperspectral data, extraction of ROIs by PCA imaging and image processing, average spectra extracted from 6 ROIs (Fruit-bottom, Fruit-top, Flesh-bottom, Flesh-top, Achene-bottom, and Achene-top).

2.2.4. PLSR modeling

The spectra and sugar content dataset for each ROI (Fruit, Flesh, achene) included 720 data samples. The training and testing sets had a 1:1 ratio because one side of each sample was chosen. 360 data points were used for training and 360 for prediction. PLSR was performed to develop a calibration model between the averaged NIR spectral data, and the Brix reference values in the training dataset. Moreover, the competitive adaptive reweighted sampling (CARS) method was employed to select the critical wavelengths (Ma et al., 2018) and improve the robustness of the model by reducing the number of variables. In the CARS program (H.-D. Li et al., 2018), the regression coefficients of the PLSR model were employed as an index to evaluate the contribution of each wavelength in the Brix prediction model. CARS were used to select N subsets of wavelengths from N sampling sequentially runs. In each sampling run, the number of wavelengths to be selected by CARS was regulated by the proposed exponentially decreasing function and by adaptive reweighted sampling. Finally, CARS was used to discover a combination of wavelengths with the lowest RMSECV. The model constructed for the training dataset was applied to the testing dataset to confirm the model's effectiveness. The number of PLS factors (LVs) was determined using the 10-holdout cross-validation (CV) method. The optimal LVs were selected for the maximum root-mean-square error (RMSE) for cross-validation (RMSECV) within the global minimum + 1 standard deviation range. The upper limit of LVs was set at 20. The quality of the PLSR model was assessed using the determination coefficient (R^2) and RMSE for calibration (R^2c and RMSEC) and prediction (R^2p and RMSEP). A good model possesses a low RMSEC,

RMSEP, and high determination coefficient (R^2c , R^2p) such that calibration and confirmation results do not diverge. The criteria are defined as follows.

$$RMSECV, RMSEC, RMSEP = \sqrt{(1/n)\sum_{i=1}^{n}(\hat{y}_i - \bar{y})^2} \quad (3)$$

$$R^2{}_c, R^2{}_p = 1 - \left\{\left(\sum_{i=1}^{n}(y_i - \hat{y})^2\right) \Big/ \left(\sum_{i=1}^{n}(y_i - \bar{y})^2\right)\right\} \quad (4)$$

2.2.5. Visualization of the sugar content distribution

The pixels corresponding to the flesh ROI in the hyperspectral images of the test data were used for sugar content visualization by applying the PLSR model constructed to estimate the Brix values. The spectra in the ROI were preprocessed by autoscaling before fitting the model, following the same procedure as that used for constructing the model. The sugar content distribution was displayed on a heat map after smoothing the image using a Gaussian filter to eliminate noise. Moreover, in the violin plot, the distribution of sugar content in the entire strawberry flesh section, bottom of the flesh, and top of the flesh could be determined from the data distribution based on kernel density estimation. In addition, the mean, median, and interquartile range played a role in assisting in the interpretation of this sugar distribution. Figure. 2-4 depicts the procedure to visualize the sugar content distribution.

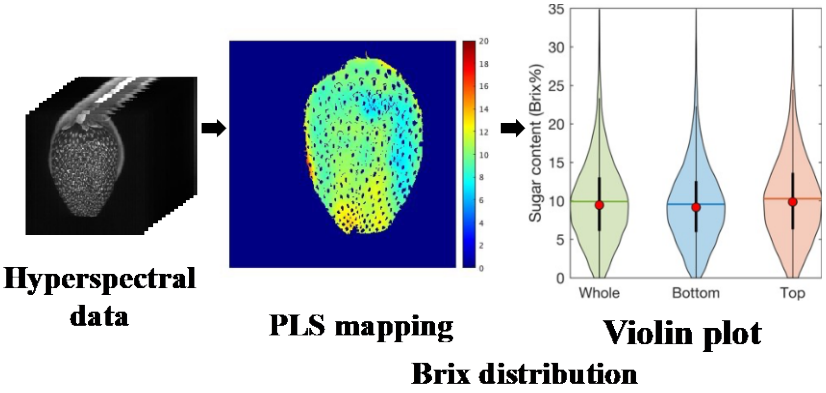

Figure 2-4. Procedure for visualization of sugar content distribution. Violin plot (colored areas: data distribution from kernel density estimation; red dots: median; black thick vertical line: interquartile range; horizontal colored lines: mean).

2.3. Results and Discussion

2.3.1. Preprocessing of hyperspectral data

Figure. 2-5 depicts PC1 loading for each sample. The PC1 loading of each sample exhibited a similar shape. In Otsu's binarization method, the threshold value that maximizes the variance between the two classes is determined and classified into two groups. This pretreatment with PC1 loading generally distinguished the flesh and achene from the fruit into two groups. This preprocessing method is considered practical because it is an automatic discrimination method that does not require a training data set and can be performed on each strawberry surface. Some samples included pixels where the reflectance was saturated owing to the Fresnel reflection of irradiated light on the unevenness of the strawberry surface. These pixels were eliminated and not used for further calculations. The mean values of the pixels assigned to the fruit, flesh, and achene parts were 29,038, 25,454, and 2367, respectively, as shown in Figure 2-6. The average ratio of the pixels corresponding to achenes in fruits was 8.7%. In addition, the distribution of the number of pixels was wide owing to variations in size and shape.

Figure 2-7 shows the average spectra of (a) fruit, (b) flesh, and (c) and achene; and their corresponding second derivative spectra ((d), (e), (f), respectively). The average spectrum had absorption peaks at 970, 1165, 1420, 1780, and 1900 nm. The peaks at 970, 1420, and 1900 nm corresponded to O–H-related water content, those at 1165 and 1780 nm corresponded to C–H and those at 1165 and 1780 nm corresponded to C–H-related sugar(Golic et al., 2003). These absorption bands have also been observed in red strawberries (Liu et al., 2019). The average spectra from the flesh part exhibited different characteristics from the achene part, i.e., the reflection at 1420 nm due to water because the water content value significantly differed between flesh and achene. The fruit and flesh spectra exhibited almost identical peak intensities because pixels of achene had a low ratio to those of the fruit, at 8.7%. Flesh and achene exhibited differences in absorption peak intensity in the second derivative spectra, particularly at 1165 nm owing to CH and 970 and 1900 nm owing to OH. Furthermore, a specific absorption peak was observed only from achene at approximately 1710 nm, which corresponds to $C–H_2$ (Golic et al., 2003).

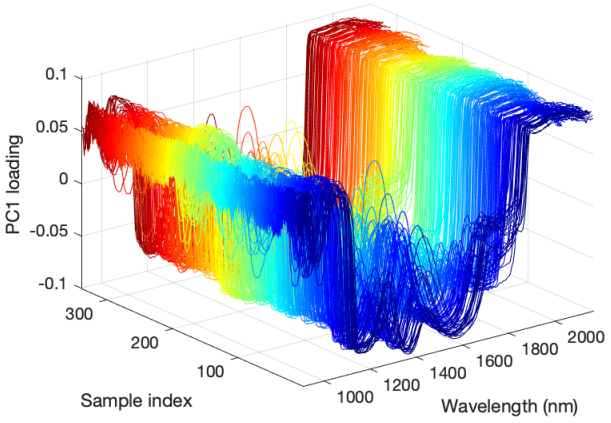

Figure 2-5. PC1 loadings of all samples obtained by principal component analysis from the pixels of the hyperspectral data measurement plane.

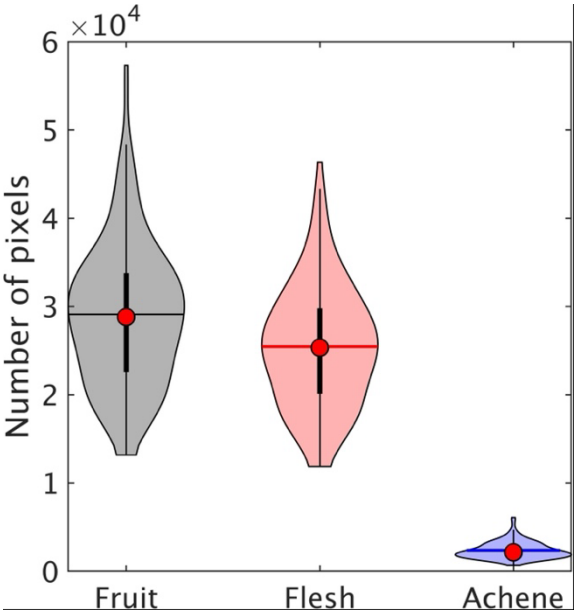

Figure 2-6. Number of pixels for ROI of fruit, flesh, and achene in strawberry, with ROIs defined by image masks created by preprocessing hyperspectral data.

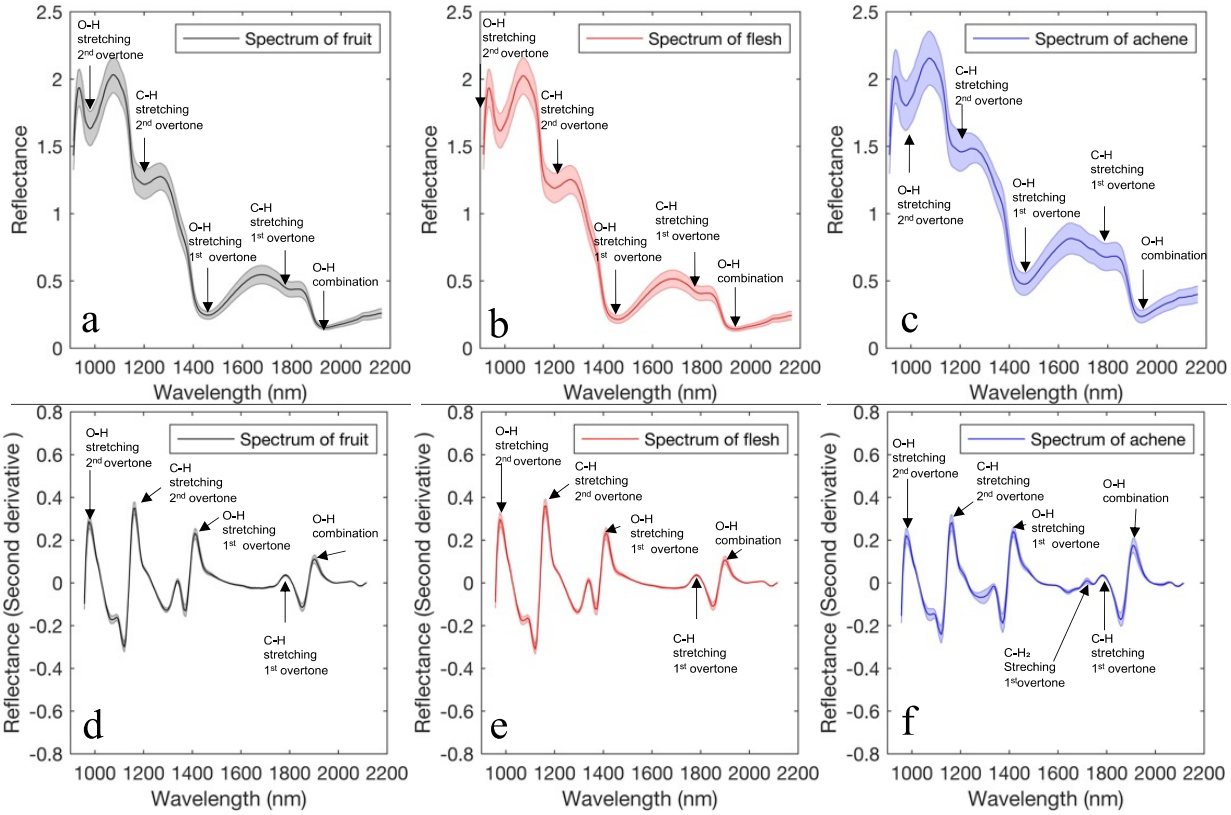

Figure 2-7. Average reflectance spectra (the spectral range is the mean ± standard deviation) of (a) fruit, (b) flesh, and (c) achene. Second derivative average reflectance spectra (Spectral range is mean ± standard deviation) of (d) fruit, (e) flesh, and (f) achene in strawberries.

2.3.2. PLSR Model

Figure. 2-8 shows the distribution of Brix reference values for strawberries in the training and testing datasets from the bottom and top parts of the strawberries. The training dataset contained a more comprehensive range of values than the testing dataset. The Brix value at the top of the fruit was higher than that at the bottom. This result indicates that white strawberries accumulate more sugar at the top of the fruit than red strawberries (Ikegaya et al., 2019).

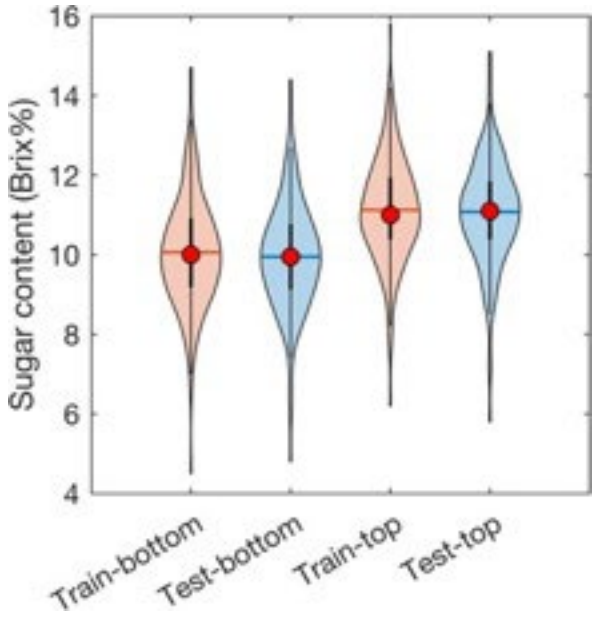

Figure 8. Sugar content (Brix%) references measured from blocks cut from the top and bottom of the fruit using a Brix meter (training dataset vs. testing dataset).

Table 2-1 summarizes the CARS-PLSR model evaluated using numerous conditions (such as spectral pretreatment and ROI used). Evidently, the model constructed from the spectra extracted from the achene ROI yielded a low value of $R^2{}_p$. We considered that the relationship between the information on achene and the information on fruit sugar accumulation was not good. Based on $R^2{}_p$, the model constructed from spectra extracted from the fruit or flesh ROI exhibited a higher prediction accuracy.

Table 2-1. Results of CARS-PLSR model search. The table is sorted in ascending $R^2{}_p$

Pretreat Method	ROI	Variable	LVs	RMSECV	RMSEC	RMSEP	$R^2{}_C$	$R^2{}_P$
SNV + 2nd derivative	Achene	49	4	1.095	1.029	1.043	0.494	0.477
2nd derivative	Achene	75	5	1.068	0.997	1.038	0.525	0.482
Raw	Achene	100	11	0.906	0.825	0.904	0.674	0.607
SNV	Achene	31	9	0.776	0.727	0.799	0.747	0.693
2nd derivative	Flesh	145	4	0.739	0.703	0.742	0.764	0.735
2nd derivative	Fruit	157	4	0.731	0.694	0.728	0.770	0.745
SNV	Flesh	37	8	0.572	0.537	0.714	0.862	0.755
SNV + 2nd derivative	Fruit	88	4	0.680	0.649	0.692	0.799	0.769
SNV + 2nd derivative	Flesh	34	5	0.691	0.645	0.683	0.801	0.775
SNV	Fruit	60	9	0.630	0.579	0.632	0.839	0.808

Raw	Fruit	26	9	0.600	0.566	0.633	0.847	0.808
Raw	Flesh	35	8	0.558	0.530	0.576	0.866	0.841

The model constructed from the raw spectra extracted from the flesh ROI had the highest prediction accuracy, with RMSEP and $R^2{}_p$ values of 0.576 and 0.841, respectively. The accuracy of the models was not much different compared with the fruit and flesh ROIs. Because the ratio of achene pixels was low (8.7%), it had less effect on the model constructed based on the averaged spectrum. Figure. 2-9 shows the wavelength selected by CARS and the relation between the measured and predicted Brix values. Raw spectra extracted from the flesh ROI were employed for the model. Figure. 2-9a depicts the 35 wavelengths (black points) selected using the CARS method. These selected wavelengths are associated with C-H (approximately 1420 and 1780 nm) and O-H (approximately 1900 nm). Figure. 2-9b depicts the relationship between the measured and predicted Brix values obtained by PLSR calibration for the training (blue) and testing dataset (red). Eight PLS factors (LVs) were selected as the optimum number for the PLSR calibration model using 35 critical wavelengths. The PLSR calibration model had substantial prediction accuracy; its $R^2{}_c$ and RMSEC were 0.866 and 0.530, $R^2{}_p$, and RMSEP were 0.841 and 0.576, respectively. Because the difference in accuracy between the calibration and prediction datasets was small, the PLSR model did not overfit the data. The prediction accuracy $R^2{}_p$, and RMSEP of a model proposed in a prior study (Liu et al., 2019), which visualized the total water-soluble sugar (TWSS) in strawberries with red skin using NIR-HSI (1000–2500 nm), were 0.774 and 6.459 mg·g^{-1}, respectively. Note that TWSS is the total amount of sugar measured using HPLC and strongly correlates with the Brix value. The PLSR model used in this study exhibited a higher prediction accuracy than prior NIR-HSI investigations. Moreover, the prediction results were equally high compared with the sugar content prediction results of FT-NIR spectrometry ($R^2{}_p$ and RMSEP were 0.85 and 0.58, respectively) (Amodio et al., 2017).

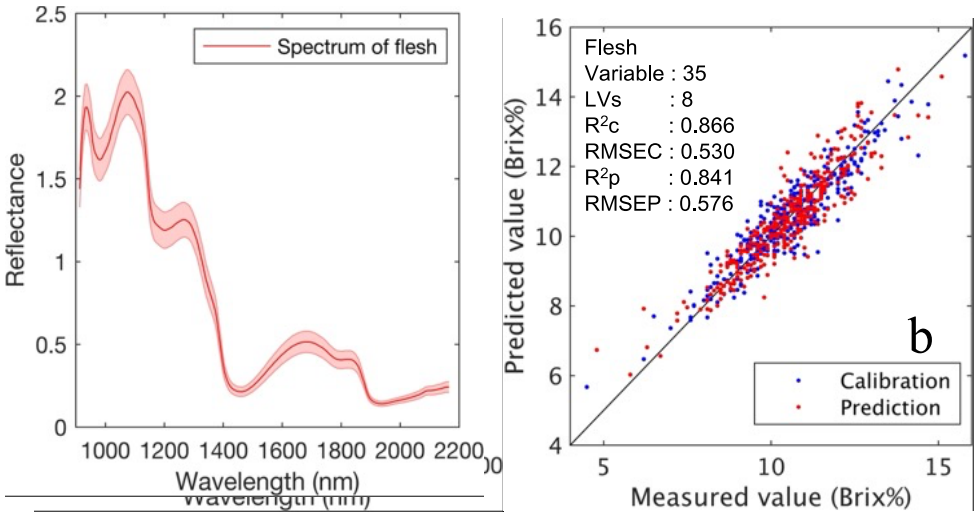

Figure 2-9. (**a**) A total of 35 key wavelengths (black points) are selected by the CARS method. (**b**) PLSR calibration results with training data set and prediction with testing dataset using the

selected 35 key wavelengths and 8 LVs; the R^2c, and RMSEC are 0.866 and 0.530, whereas R^2p and RMSEP are 0.841 and 0.576, respectively.

2.3.3. Visualization of the Sugar Content Distribution

Figure. 2-10 depicts heatmap images of Brix prediction for each flesh ROI using the developed PLSR model and violin plots denoting the distribution of pixel Brix values for the whole fruit, bottom, and top. In order to display representative samples, samples were selected from the lowest to the highest sugar content and arranged in alphabetical order. The color scale indicates the predicted Brix values of the strawberries. Using the flesh ROI mask, our heatmap and violin plot remove approximately 8.7% (ratio of achene pixels) of unnecessary pixel information for the flesh of fruit surface evaluation. The differences between the Brix values for each strawberry were successfully visualized. In an earlier study (Weng et al., 2020b; Liu et al., 2019), the characteristics of the flesh parts could not be observed owing to the color of the achene. By contrast, local flesh parts' sugar content variations were observed in our heatmap images.

Furthermore, violin plots showed the sugar content distribution of the flesh in the whole fruit, bottom, and top. The heatmap images have the benefit of assessing Brix size and distribution. Simultaneously, violin plots helped to statistically determine the differences in Brix between samples and sample parts. Visualizing spatial distribution and violin plots is an excellent way to evaluate strawberries that can be offered to consumers or used as a selection criterion. Because the wavelength (913–2166 nm) of NIR-HSI used in the proposed method does not depend on pigment information, such as anthocyanin, this evaluation method can also be applied to red strawberries.

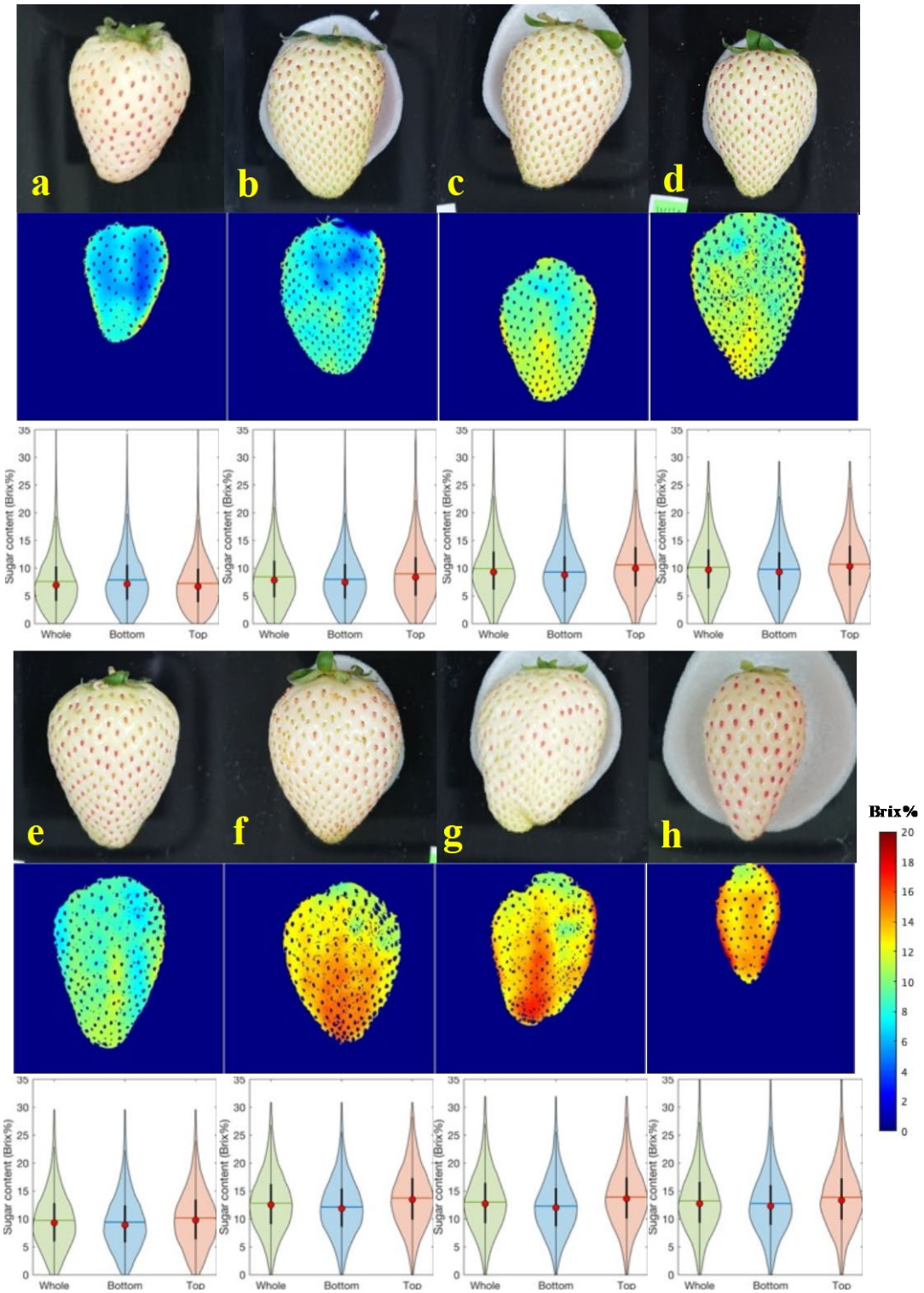

Figure 2-10. Prediction images and violin plots of Brix values using the PLSR model for white strawberries. Violin plots represent the distribution of pixel Brix values for each ROI (whole flesh, bottom flesh, and top flesh). In order to display representative samples, samples were selected from the lowest to the highest sugar content and arranged in (a-h) order.

2.4. Conclusion

This study proposed a new method to evaluate white strawberries' sugar content using NIR-HSI. The PCA imaging as preprocessing method combining PCA and image processing was developed to separate flesh and achene on the fruit surface automatically. The PLSR model constructed from the raw spectra extracted from the flesh ROI exhibited good prediction accuracy with RMSEP and R^2_p of 0.576 and 0.841, respectively, and included a relatively low number of PLS factors. This model demonstrated good prediction performance. The characteristics of the sugar content distribution in the flesh of white strawberries were depicted using the produced Brix heatmap images and violin plots.

These findings suggest that NIR-HSI can be used for noncontact evaluation of the quality of white strawberries. The key advantage of NIR-HSI is its ability to assess fruit without damaging it. Suppose the HSI data of strawberries growing in the field can be measured over time. In that case, novel criteria for judging ripeness from visualization of variations in the distribution of Brix values can be developed. Although we focused on Brix as a measure of sugar content in this research, the same approach can be extended to other quality indicators, such as acidity, hardness, and damage, by increasing the number of objective variables.

3. 3D sugar content imaging of strawberries by Near-infrared hyperspectral imaging and laser displacement measurement

3.1. Introduction

The sugar content distribution within a fruit is known to be uneven. Presently, market measurements of sugar content in fruits like apples and mandarin oranges utilize near-infrared spectroscopy, which offers non-destructive molecular vibration information. However, this technique only provides an average sugar content per fruit, without evaluating spatial distribution.

Recently, extensive research has been conducted on NIR-HSI (near-infrared hyperspectral imaging) for evaluating the quality of agricultural products and mapping chemical components. NIR-HSI captures near-infrared spectra as images, with each pixel representing a spectrum. Thus, it facilitates the visualization of sugar content distribution by estimating the sugar content from each pixel's near-infrared spectrum. Earlier studies using NIR-HSI often used flat samples. For instance, they measured the cross-section of an apple sliced at the equatorial plane. The difficulty arises from the Fresnel reflection of irradiated light in the sample's uneven areas, which alters reflectance, complicating the evaluation of the reflectance spectrum. Furthermore, variations in detector distance based on the sample area hinder uniform reflectance evaluation. This poses a challenge for the application of NIR-HSI in assessing the sugar content of fruits, given their circular shape and uneven surfaces. The limitation of NIR-HSI, with its propensity for flat sample measurements, was mitigated by integrating it with 3D shape measurement. First, a high-precision laser displacement meter simultaneously measures the 3D shape data of the fruits to derive NIR-HSI data. The spectral data stored in each pixel is then corrected using this 3D shape data as variables, considering fruit curvature and camera distance. This ensures a stable visualization of the fruit's quality across its surface. The present research centers on strawberry fruit. It non-destructively and precisely models the sugar content distribution on the fruit's surface in 3D, using shape information to correct the spectrum of each pixel in the near-infrared hyperspectral data. The findings will permit non-destructive quality evaluation of individual strawberries and their constituent parts.

3.2. Materials and Methods

3.2.1. Hyperspectral data and shape data measurement and Brix measurements

In this study, 193 strawberries of the "Tochigi i37" variety from Tochigi Prefecture, Japan, were procured. These samples were transported under refrigeration and stored at a temperature of 5°C until one hour prior to the experiment. Subsequently, they were maintained at a constant temperature of 23°C in a laboratory setting. Notably, some strawberries incurred minor damage during transport. Each sample was bifurcated, selecting the unblemished side for subsequent measurements. The measurement apparatus incorporated a Near-Infrared Hyperspectral Imaging (NIR-HSI) system (push-broom line scanning system: Compovision, Sumitomo Electric Industries, Ltd., Tokyo, Japan), a light source, a laser displacement meter (LJ-X8200, KEYENCE, Ltd., Osaka, Japen), and a sliding table (Figure. 3-1). he NIR-HSI system featured a spectroscope and a 2D photosensitive element capable of intercepting Near-Infrared (NIR) light between 913 and 2519 nm at intervals of 6.2 nm. The tubular light source, equipped with four halogen lamps, afforded illumination from both directions. The irradiation angle was calibrated at 45°. The laser displacement meter uses a 405nm laser with a profile data count of 3200 points and a Z-axis repeatability of 1 μ m. The NIR-HSI frame rates were set to 150 frames s^{-1}, 320 frames s^{-1}, and 320 frames s^{-1} for sample, dark, and white, respectively. Samples were placed on precisely cut aluminum blocks (Width:60mm, Length:70mm) or line-scan measurements, the samples were positioned on accurately machined aluminum blocks. This procedure facilitated alignment of the hyperspectral data procured from the NIR-HSI with the shape data acquired via the laser displacement meter. A black sheet adhered to the surface of the aluminum block to optimize image processing. The laser and hypers field of view was calibrated to reflect the reference rectangular block. The laser displacement meter operated at a measurement velocity of 2.5 mm/sec. To preclude light interference, dark data measurements were conducted with the lens cap sealed. The reference board was stationed at a height of 10 mm from the block for measurement.

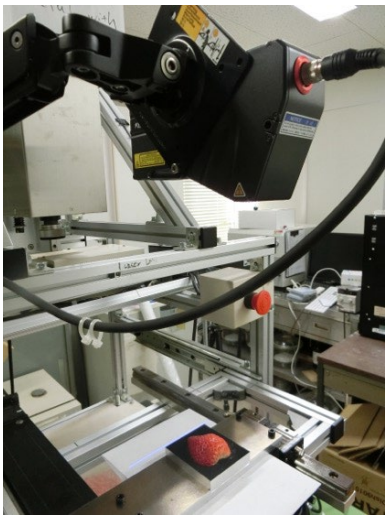

Figure 3-1. Strawberry line scan measurement system using NIR-HSI system and laser displacement meter

3.2.2. Pre-processing of hyperspectral data and shape data

Figure.3-2 shows the method of shape correction (height correction and angle correction) of Hyperspectral data using shape data. The data was first cut out based on the measurement block to match the coordinates of the measured hyperspectral data and shape data. In addition, the shape data was resized based on the data size of the hyperspectral data.

The correction of Hyperspectral data was that the shape correction was considered separately for distance and angle. For height, the correction was based on the law of light decay, and for angle, a correction formula based on the Lambert Cosine law was used. The patterns are height, angle, and height and angle. Shape uncorrected reflectance ($R_{non-correct}$) was calculated from sample, white, and dark data according to Equation (3-1). The height-corrected reflectance ($R_{height-correct}$) was calculated by Equation (3-3) using the height-corrected sample intensity ($I_{height-correct}$) calculated by Equation (3-2). Equation (3-2) was formulated regarding the inverse-square law of light decay. The distance from the light source to the reference board (H_{light}) was 100 mm, and from the reference board to the hyperspectral camera (H_{camera}) was 200 mm, applying actual measurements. Angle-corrected sample intensity ($I_{angle-correct}$) was calculated using equation (3-4) for angle correction by Lambert's cosine law. The intensity of the sample with the combination of height and angle correction ($I_{height\&angle-correct}$) was calculated by Equation (3-6), and the reflectance ($R_{height\&angle-correct}$) after height and angle correction was calculated by Equation (3-7).

$$R_{non-correct} = \frac{I-dark}{white-dark} \quad (3\text{-}1)$$

$$I_{height-correct} = \frac{I-dark}{\left(\frac{H_{light}+x}{H_{light}}\right)^2 \cdot \left(\frac{H_{camera}+x}{H_{camera}}\right)^2} \quad (3\text{-}2)$$

$$R_{height-correct} = \frac{I_{height-correct}}{white-dark} \quad (3\text{-}3)$$

$$I_{angle-correct} = \frac{I-dark}{\cos\theta} \quad (3\text{-}4)$$

$$R_{angle-correct} = \frac{I_{angle-correct}}{white-dark} \quad (3\text{-}5)$$

$$I_{height\&angle-correct} = \frac{I_{height-correct}}{\cos\theta} \quad (3\text{-}6)$$

$$R_{height\&angle-correct} = \frac{I_{height\&angle-correct}}{white-dark} \quad (3\text{-}7)$$

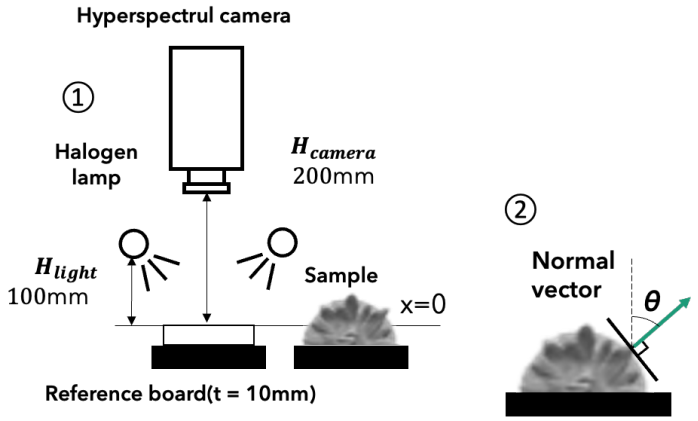

Figure 3-2. Overview of height and angle correction using NIR-HSI geometry data

3.2.3. PLSR modeling

PLSR constructed a sugar content model for the spectral and sugar content data. The data set was split 7:3 into training and test sets for model building and evaluation. The model construction optimized the number of PLS factors by 5-hold-out cross-validation for the training set. The optimal LVs were selected for the maximum root-mean-square error (RMSE) for cross-validation (RMSECV) within the global minimum + 1 standard deviation range. The quality of the PLSR modl was assessed using the determination coefficient (R^2) and RMSE for calibration (R^2c and RMSEC) and prediction (R^2p and RMSEP). A good model possesses a low RMSEC, RMSEP, and high determination coefficient (R^2c , R^2p) such that calibration and confirmation results do not diverge.

3.2.4. 3D sugar content imaging

A 3D image was created by combining the sugar content image and shape data. To evaluate the results, we decided to use the newly created Map Score as an index (3-8); the Map Score is a multiplication of three evaluation parameters. The coefficient of determination of the sugar level estimation model, the average value of the sugar level calculated from the actual squeezed sugar level and the corresponding captured image, and the percentage of pixels that fall within the sugar level range in the training data when constructing the PLS model. Since the closer the values of all three parameters are to 1, the better the parameter, we conclude that the higher the Mapscore, the better.

$$\text{Mapscore} = R^2{}_p \times \rho(y,\hat{y}) \times \mu_{\rho\_px\_model} \times 100 \quad (3\text{-}8)$$

$\boldsymbol{R^2_p}$:Coefficient of determination for model creation (test set), $\boldsymbol{\rho(y,\hat{y})}$:correlation coefficient（Actual values at the top and bottom of strawberry fruit as measured by a sugar meter Actual values at the top and bottom of strawberry fruit as measured by a sugar meter VS Average sugar content of ROIs (at the top and bottom of the flesh) calculated from the mapping results of the fruit flesh.）,$\boldsymbol{\mu_{\rho\_px\_model}}$:Pixel Ratio（Number of pixels that fell within the range of guaranteed prediction accuracy when creating the model for the training set (minimum to maximum sugar values for the training set) vs. number of pixels in the fruit flesh ROI).

As an output evaluation in NIR-HSI, we propose the strawberry deviation value as Tscore (3-9), since it can only be judged visually in imaging images. Deviation is an index used in school testing and quality control in the manufacturing industry, where the average is 50 and one can intuitively judge how far away from it one is. The mean and standard deviation here are calculated from the training set of model creation, and if the training set has sufficient sampling, it can be used as a basis for value judgment.

$$Tscore = \frac{Mapping\_Brix - \mu_{train}}{\sigma_{train}} \times 10 + 50 \quad (3\text{-}9)$$

3.3. Results and Discussion

3.3.1. Effect of shape correction on the average spectrum

Figure 3-3. show the spectral images of one sample strawberry in the row direction with no correction, height correction, angle correction, height & angle correction, and in the column direction at the major absorption wavelengths. The correction has changed the characteristics of the spectral images. The figure shows the average spectra of all samples before and after correction. The average spectrum shows that the height correction is weaker, the angle correction is stronger than without correction, and the height and angle corrections are slightly stronger. This also shows the possibility of spectral correction for shape data, whereas up to now we have only corrected for shape in the spectral preprocessing.

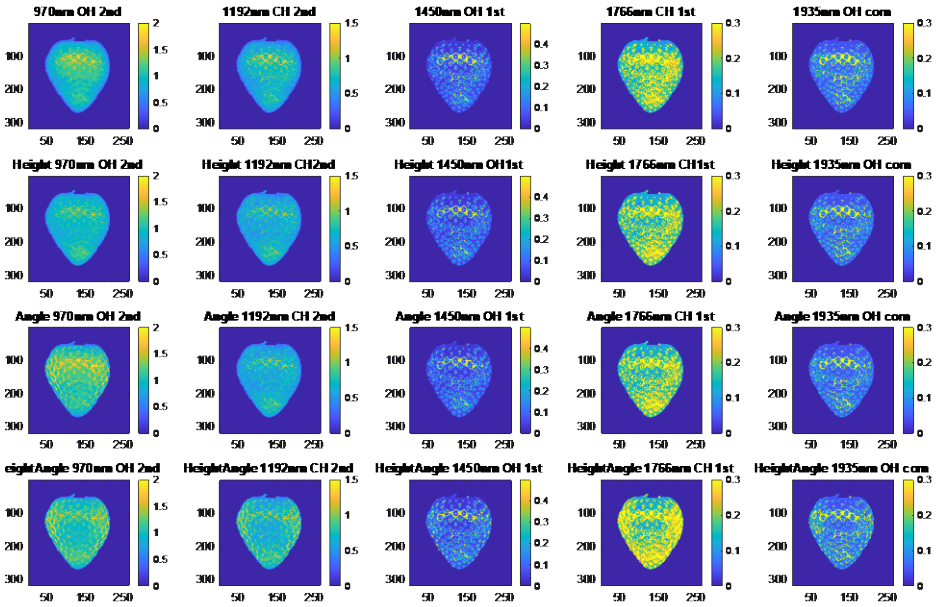

Figure 3-3. Spectral images in the main bands of strawberry showing the effect of shape correction

The average spectra before and after shape correction for all samples are shown in Figure. 3-4. The average spectra were calculated using flesh ROIs created by PCA imaging. The height correction tended to decrease the overall reflectance of the spectrum, while the angle correction tended to increase the overall reflectance. The combination of height and angle correction tended to slightly increase reflectance compared to no shape correction.

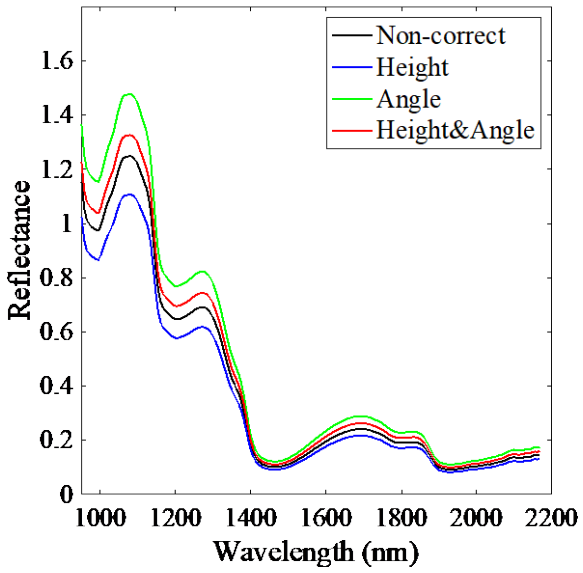

Figure 3-4. The average spectrum of measured strawberry samples. Calculated from the flesh ROI before and after shape correction.

3.3.2. PLSR model

The table summarizes the results of the PLS model search. Comparing the coefficients of determination for the test set, the model with smoothing after height correction showed the best prediction accuracy with a coefficient of determination of 0.813 and PMSEP of 0.687 for the test set.

Table 3-1. Results of PLSR model search

Shape correction	Spectral processing	LV	RMSECV	RMSEC	RMSEP	R^2_{CV}	R^2_C	R^2_P
Non-correct	-	6	0.710	0.691	0.738	0.795	0.807	0.785
Non-correct	Smoothing	6	0.680	0.661	0.736	0.812	0.823	0.786
Non-correct	1st derivative	4	0.682	0.658	0.793	0.812	0.824	0.751
Non-correct	2nd derivative	4	0.644	0.614	0.699	0.832	0.847	0.806
Non-correct	SNV	6	0.674	0.645	0.778	0.816	0.831	0.761
Non-correct	SNV-Smoothing	5	0.705	0.676	0.820	0.799	0.814	0.734
Non-correct	SNV-1st derivative	3	0.705	0.684	0.827	0.799	0.810	0.729
Non-correct	SNV-2nd derivative	3	0.654	0.626	0.734	0.826	0.841	0.787
Height	-	7	0.694	0.652	0.741	0.805	0.828	0.783
Height	Smoothing	7	0.667	0.631	0.727	0.820	0.839	0.791
Height	1st derivative	3	0.723	0.700	0.792	0.788	0.801	0.751
Height	2nd derivative	3	0.754	0.742	0.755	0.770	0.777	0.775
Height	SNV	6	0.649	0.623	0.739	0.829	0.843	0.784
Height	SNV-Smoothing	6	0.689	0.658	0.791	0.808	0.824	0.752
Height	SNV-1st derivative	4	0.706	0.627	0.726	0.798	0.841	0.791
Height	SNV-2nd derivative	3	0.666	0.636	0.732	0.820	0.836	0.788
Angle	-	6	0.705	0.683	0.715	0.798	0.811	0.798
Angle	Smoothing	6	0.679	0.657	0.707	0.813	0.825	0.802
Angle	1st derivative	4	0.674	0.649	0.764	0.816	0.829	0.769
Angle	2nd derivative	3	0.784	0.763	0.770	0.751	0.764	0.765
Angle	SNV	6	0.653	0.626	0.751	0.827	0.841	0.776
Angle	SNV-Smoothing	5	0.714	0.685	0.823	0.793	0.810	0.732
Angle	SNV-1st derivative	3	0.719	0.694	0.836	0.791	0.804	0.723
Angle	SNV-2nd derivative	2	0.758	0.744	0.773	0.767	0.775	0.764
Height+Angle	-	7	0.670	0.635	0.720	0.818	0.837	0.795
Height+Angle	Smoothing	7	0.630	0.600	0.687	0.839	0.854	0.813
Height+Angle	1st derivative	3	0.719	0.696	0.768	0.790	0.803	0.767
Height+Angle	2nd derivative	3	0.738	0.679	0.710	0.779	0.813	0.801

Height+Angle	SNV	6	0.632	0.598	0.711	0.838	0.855	0.800
Height+Angle	SNV-Smoothing	6	0.682	0.655	0.787	0.811	0.826	0.755
Height+Angle	SNV-1st derivative	3	0.728	0.703	0.847	0.785	0.800	0.716
Height+Angle	SNV-2nd derivative	3	0.670	0.639	0.738	0.818	0.834	0.784

3.3.3. 3D sugar content imaging

The figure shows the mapping under the conditions used in the model search. Sample A is the mapping result of the sample with high sugar content and sample B is the mapping result of the sample with low sugar content. The spectral processing changes the appearance of the mapping. In particular, the second derivative process clearly makes the image noisier. Since the PLSR model is constructed from the average spectrum, the PLS model indicators cannot evaluate the image sharpness and noise level. unnecessary spectral preprocessing should be avoided because it amplifies the noise.

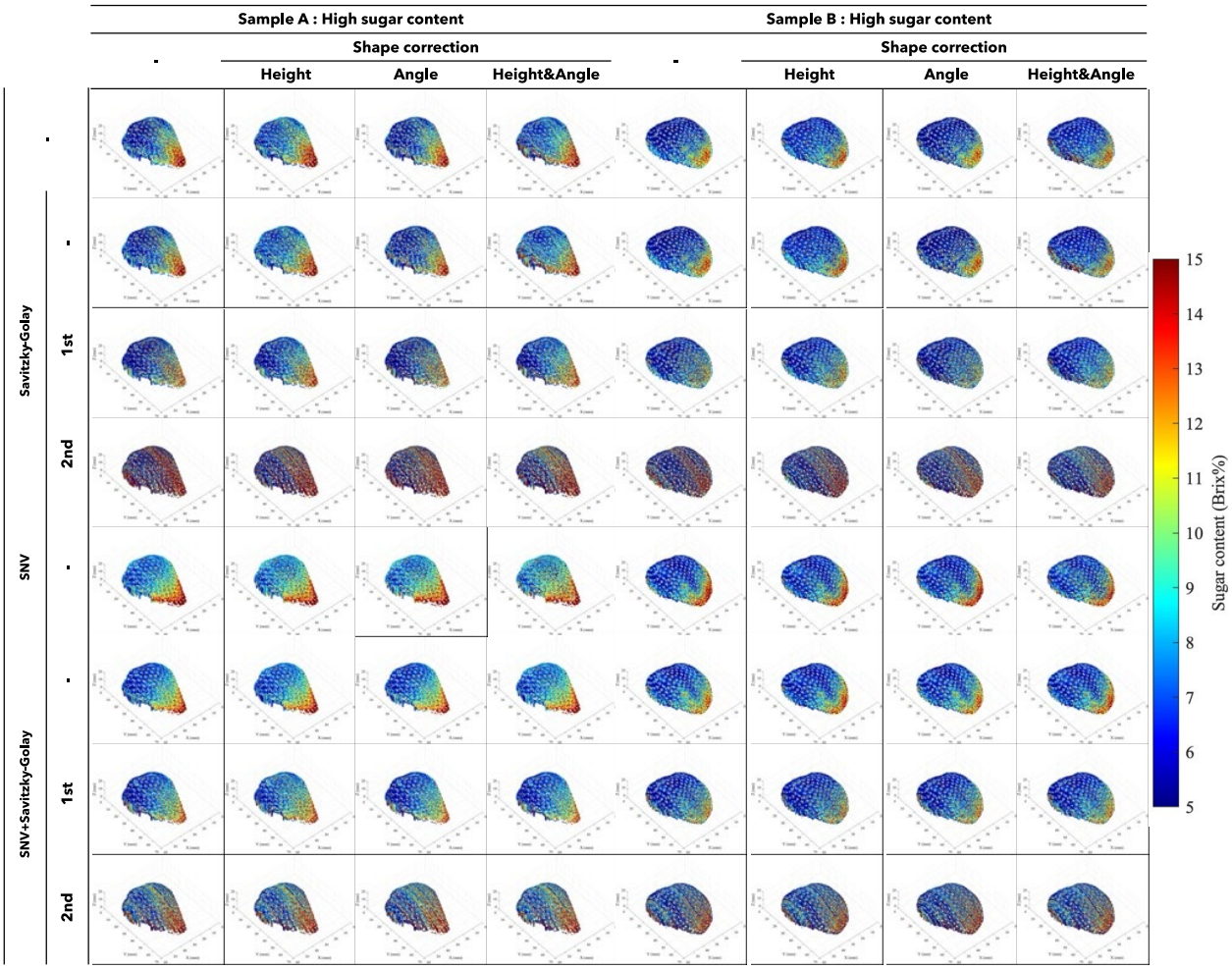

Figure 3-5. Sugar content mapping results by PLSR model per shape correction and spectral pretreatment. Sample A has high sugar content and sample B has low sugar content.

3.3.4. Evaluation of PLS mapping image

The table. 3-2 shows the map scores for each spectral condition (shape correction, spectral preprocessing) at the time of model creation. The figure. 3-6 also shows the imaging results for Sample A and Sample B for the condition with the largest map score (Height corrected and smoothing spectral preprocess), the condition with the largest coefficient of determination R^2p (Height and angle corrected and smoothing spectral preprocessed), and the condition with the lowest map score (No shape correction and 2nd derivative spectral preprocessing).

Table 3-2. Results of Mapscore .

Shape correct	Spectral processing	R^2_P	ρ	$\mu_{\rho\_px\_model}$	Mapscore
Height	Smoothing	0.791	0.92	0.73	52.52
Height	-	0.783	0.91	0.74	52.38
Height + Angle	SNV	0.800	0.92	0.71	52.33
Height	SNV	0.784	0.91	0.73	51.97
Height + Angle	SNV-Smoothing	0.755	0.90	0.75	50.82
Height	SNV-Smoothing	0.752	0.89	0.75	50.56
Angle	SNV	0.776	0.91	0.72	50.40
Non-correct	SNV	0.761	0.89	0.74	50.15
Non-correct	-	0.785	0.89	0.72	49.69
Non-correct	SNV-Smoothing	0.734	0.88	0.76	49.14
Height + Angle	-	0.795	0.89	0.69	49.10
Angle	SNV-Smoothing	0.732	0.88	0.76	48.78
Non-correct	Smoothing	0.786	0.89	0.69	48.51
Height Angle	1st derivative	0.767	0.90	0.70	48.32
Angle	-	0.798	0.88	0.68	48.15
Height + Angle	Smoothing	0.813	0.89	0.66	48.05
Height	SNV-1st derivative	0.791	0.90	0.67	47.59
Height	1st derivative	0.751	0.89	0.71	47.44
Height + Angle	SNV-1st derivative	0.716	0.88	0.72	45.25
Non-correct	SNV-1st derivative	0.729	0.88	0.70	44.69
Angle	SNV-1st derivative	0.723	0.88	0.70	44.43
Angle	Smoothing	0.802	0.86	0.63	43.68
Angle	1st derivative	0.769	0.90	0.60	41.21
Non-correct	1st derivative	0.751	0.89	0.61	40.91
Height+Angle	SNV-2nd derivative	0.784	0.90	0.56	39.57
Height	SNV-2nd derivative	0.788	0.89	0.55	38.93
Non-correct	SNV-2nd derivative	0.787	0.88	0.54	37.33
Height+Angle	2nd derivative	0.801	0.91	0.50	36.31
Angle	SNV-2nd derivative	0.764	0.88	0.54	36.04
Angle	2nd derivative	0.765	0.87	0.47	31.19
Height	2nd derivative	0.775	0.89	0.45	31.17
Non-correct	2nd derivative	0.806	0.88	0.41	29.07

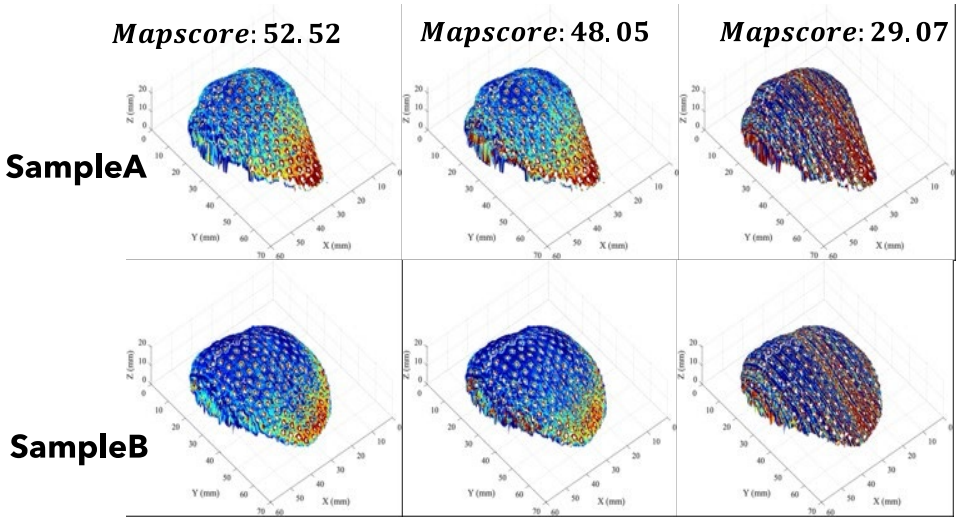

Figure 3-6. Comparison of mapping results by Mapscore

3.3.5. Proposal of strawberry evaluation method by hyperspectral imaging.

Deviation values at the top and bottom of the fruit were calculated from sample A, which had high and low sugar content, and sample B, which had low sugar content (Figure). The difference between samples and the possible values of the sugar content of strawberries at the time of training was determined. In this study, we used the average value of the apex and the base of the fruit, but we are still working on expanding the evaluation method to make use of more spatial information.

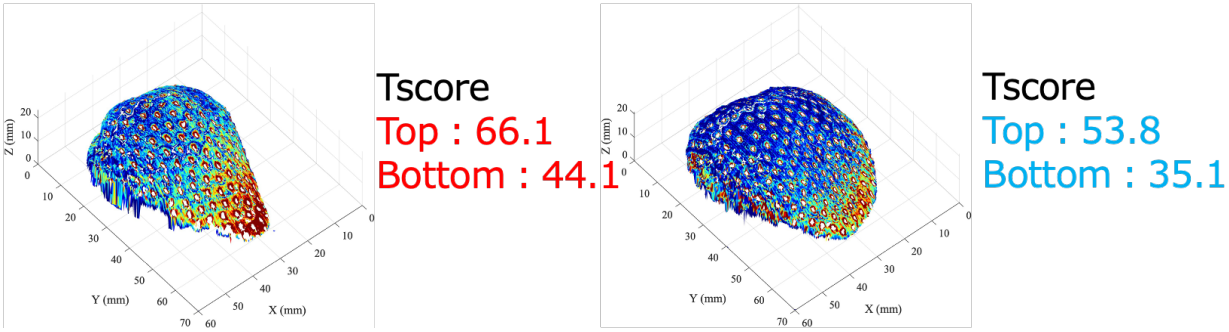

Figure 3-7. Strawberry line scan measurement system using NIR-HSI system and laser displacement meter

3.4. Conclusion

In Chapter 3, The system combining the HIR-HSI system and shape measurement by laser displacement meter was constructed for imaging sugar content in 3D by correcting the weak point of NIR-HSI, i.e., shape. In the shape correction, the combination of height and angle and height and angle correction methods showed the possibility of spectral processing methods other than spectral preprocessing. Only the predictive performance of PLSR models has been evaluated for PLS mapping, but in this study, the mapping method was optimized using the developed evaluation index Mapscore. A strawberry deviation value (Tscore) was also proposed to interpret the sugar content values estimated by nondestructive evaluation.

4. 3D sugar content imaging model of the whole strawberry surface by Near-infrared hyperspectral imaging and shape rotation measurements

4.1. Introduction

In Chapter 2, Principle Component Analysis (PCA) imaging was utilized with Hyperspectral data to discriminate the strawberry flesh from the remainder of the fruit, consequently generating an image exclusive to the sugar content of the flesh. In the subsequent chapter, Near-Infrared Hyperspectral Imaging (NIR-HSI) was amalgamated with laser displacement measurement, facilitating the correction of the spectral shape and yielding a three-dimensional visualization of the sugar content within the strawberry flesh. Nevertheless, the employed line-scan method permits measurement of merely one facet of the strawberry at a time, thus precluding the portrayal of the flesh's sugar content distribution across the entire fruit surface. It is imperative to note that variations in sugar content manifest in axial and equatorial directions within strawberries, with the sun-exposed side exhibiting elevated sugar content(Ikegaya et al., 2019). Consequently, comprehensive fruit surface information acquisition is desirable. While previous studies have employed point cloud information for full-surface three-dimensional strawberry measurements (He et al., 2017), none have rendered the sugar content of the entire strawberry surface in three dimensions. In this study, NIR-HSI and shape measurements were integrated with rotational scanning to secure data concerning the whole strawberry surface. Point cloud information for three-dimensional measurements necessitates acquiring numerous images from varied viewpoints. In the other hand, Rotational scanning considerably expedites the process.

4.2. Materials and Methods

4.2.1. Rotation hyperspectral data and shape data measurement and Brix measurements

Strawberry samples were 193 fruits of the variety “Tochigi i37” from Tochigi Prefecture, Japan, purchased from farmers. The strawberries were transported by refrigerated delivery and kept after refrigeration (5°C) until approximately 1 hour before the experiment. Before the experiment, they were kept in the laboratory (23°C) to keep the product temperature constant. Some samples were slightly damaged during transport. The measurement system comprises The NIR hyperspectral imaging system (push-broom line scanning system: Compovision, Sumitomo Electric Industries, Ltd., Tokyo, Japan), The light source, The laser displacement meter (LJ-X8200, KEYENCE, Ltd., Osaka, Japen), and the turn table (OSMS-40YAW, Sigumakoki, Co., Ltd., Tokyo, Japan). The

NIR-HSI system was equipped with a spectroscope and a 2D photosensitive element (256 pixels (wavelength) × 320 pixels (position)) capable of receiving NIR light from 913 to 2519 nm at a spectral interval of 6.2 nm. The light source was tube-shaped and illuminated from both sides using four halogen lamps. The irradiation angle was adjusted to 45°. The laser displacement meter uses a 405nm laser with a profile data count of 3200 points and a Z-axis repeatability of 1 μ m. The NIR-HSI frame rates were set to 100 frames s^{-1}, 100 and 320 frames s^{-1}, and 320 frames s^{-1} for sample, dark, and white, respectively. The NIR-HSI system and laser displacement meter were used to measure hyperspectral images and shape data for one turntable rotation. Reference data was obtained by measuring the reference board every 2 mm from 0 mm to 30 mm in height with the center of rotation of the turntable as the origin. Dark data were measured with the lens cap closed to prevent light from entering the detector.

Figure 4-1. Strawberry Rotation line scan measurement system using NIR-HSI system and laser displacement meter

4.2.2. Pre-processing of hyperspectral data and shape data

Figure.4-2 shows the method of shape correction (height correction and shape correction) of Hyperspectral data using shape data. The data was first cut out based on the measurement block to match the coordinates of the measured Hyperspectral data and shape data. In addition, the shape data was resized based on the data size of the hyperspectral data.

The correction of Hyperspectral data was that the shape correction was considered separately for distance and angle. For the height correction, the measured values of the reference board at different heights were used. for the angle, a correction formula based on the Lambert Cosine law was used. The patterns are height, angle, and height and angle. Shape uncorrected reflectance ($R_{non-correct}$) was calculated from sample, white, and dark data according to Equation (4-1). The reflectance ($\boldsymbol{R_{height-correct}}$) after height correction was calculated using Equation (4-2). Angle-corrected reflectance ($\boldsymbol{R_{angle-correct}}$) was calculated with Lambert Cosine correction using Equation (4-3). The reflectance ($\boldsymbol{R_{height\&angle-correct}}$) after the combined height and angle correction was calculated by Equation (4-4).

$$\boldsymbol{R_{non-correct}} = \frac{\boldsymbol{I-dark}}{\boldsymbol{white-dark}} \qquad (4\text{-}1)$$

$$\boldsymbol{R_{height-correct}} = \frac{\boldsymbol{I-dark}}{\boldsymbol{white_{height-correct}-dark}} \qquad (4\text{-}2)$$

$$\boldsymbol{R_{angle-correct}} = \frac{\frac{\boldsymbol{I-dark}}{\boldsymbol{\cos\theta}}}{\boldsymbol{white-dark}} \qquad (4\text{-}3)$$

$$\boldsymbol{R_{height\&angle-correct}} = \frac{\frac{\boldsymbol{I-dark}}{\boldsymbol{\cos\theta}}}{\boldsymbol{white_{height-correct}-dark}} \qquad (4\text{-}4)$$

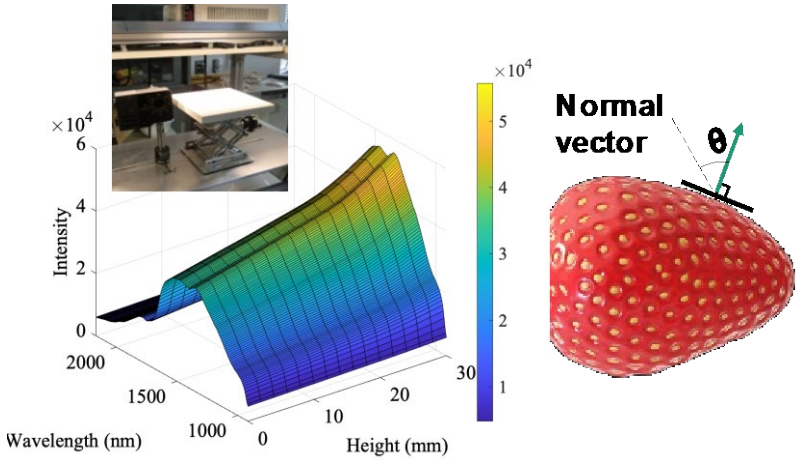

Figure 4-2. Overview of height and angle correction using NIR-HSI geometry data

4.2.3. PLSR modeling

PLSR constructed a sugar content model for the spectral and sugar content data. The data set was split 7:3 into training and test sets for model building and evaluation. The model construction optimized the number of PLS factors by 5-hold-out cross-validation for the training set. The optimal LVs were selected for the maximum root-mean-square error (RMSE) for cross-validation (RMSECV) within the global minimum + 1 standard deviation range. The quality of the PLSR modl was assessed using the determination coefficient (R^2) and RMSE for calibration (R^2c and RMSEC) and prediction (R^2p and RMSEP). A good model possesses a low RMSEC, RMSEP, and high determination coefficient (R^2c , R^2p) such that calibration and confirmation results do not diverge.

4.2.4. 3D sugar content imaging

The developed PLSR model was fitted to each pixel of the Hyperspectral data of the test set sample to create a sugar content mapping image. Figure. 4-3 shows an overview of 3D modeling with shape data and sugar imaging images. Since the mapping image is one rotation, it was given an angle and combined with the shape data to create a 3D model.

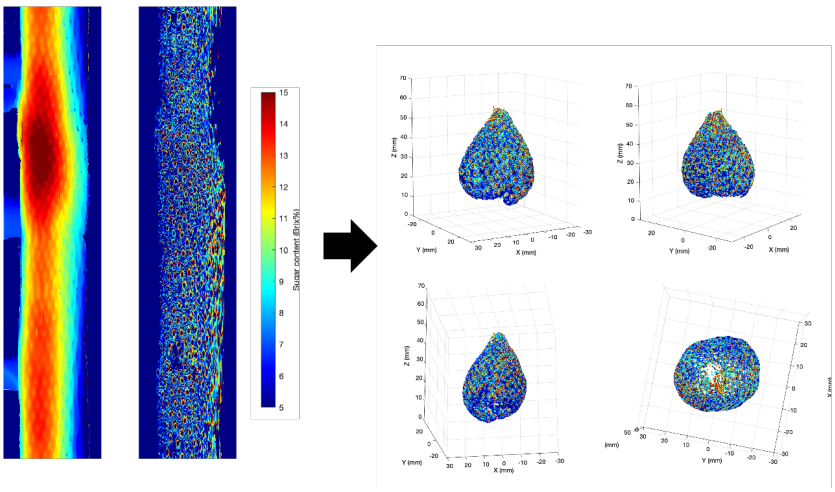

Figure 4-3. Strawberry line scan measurement system using NIR-HSI system and laser displacement meter

4.3. Results and Discussion

4.3.1. Effect of shape correction on the average spectrum

The average spectral results pre and post-shape corrections for all samples are depicted in Figure 4-4. The computation of these average spectra employed flesh-based Regions of Interest (ROIs), established through PCA imaging. The application of height correction demonstrated a general decline in the overall reflectance of the spectrum, conversely, the angle correction manifested an elevation in reflectance. The co-application of height and angle corrections induced a marginal escalation in reflectance in contrast to the absence of shape corrections. These observations remain in alignment with the results presented in Chapter 3.

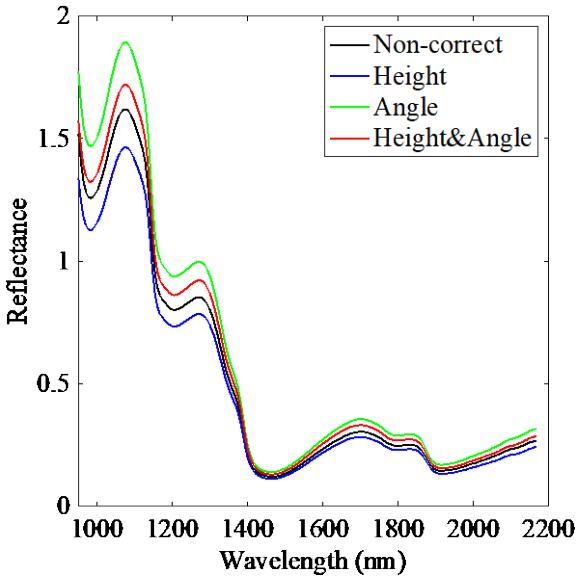

Figure 4-4. The average spectrum of measured strawberry samples. Calculated from the flesh ROI before and after shape correction.

4.3.2. PLSR model

Table. 4-1 summarizes the results of the PLS model search. The models for all conditions (shape correction and spectral pretreatment) had good prediction accuracy with R^2p greater than 0.85. Comparing the coefficients of determination for the test set, the model with SNV-2nd derivative after height correction showed the best prediction accuracy with a coefficient of determination of 0.919 and PMSEP of 0.436 for the test set.

Table 4-1. Results of PLSR model search.

Corecct	Spec treat	LV	RMSE CV	RMSE C	RMSE P	$R2_{CV}$	R^2_C	R^2_P
Non-correct	-	7	0.508	0.460	0.509	0.907	0.924	0.889
Non-correct	Smoothing	7	0.487	0.445	0.487	0.915	0.929	0.899
Non-correct	1st derivative	6	0.499	0.462	0.520	0.910	0.923	0.885
Non-correct	2nd derivative	5	0.531	0.475	0.464	0.899	0.919	0.908
Non-correct	SNV	8	0.471	0.430	0.485	0.920	0.933	0.900
Non-correct	SNV-Smoothing	8	0.482	0.440	0.498	0.917	0.930	0.894
Non-correct	SNV-1st derivative	7	0.447	0.411	0.475	0.928	0.939	0.904
Non-correct	SNV-2nd derivative	4	0.531	0.547	0.458	0.899	0.892	0.911
Height	-	8	0.498	0.456	0.522	0.911	0.925	0.884
Height	Smoothing	8	0.486	0.449	0.503	0.915	0.927	0.892
Height	1st derivative	7	0.490	0.451	0.474	0.914	0.927	0.904
Height	2nd derivative	4	0.602	0.545	0.474	0.870	0.893	0.904
Height	SNV	7	0.544	0.540	0.589	0.893	0.895	0.852
Height	SNV-Smoothing	8	0.487	0.446	0.544	0.915	0.929	0.874
Height	SNV-1st derivative	7	0.458	0.426	0.490	0.925	0.935	0.898
Height	SNV-2nd derivative	4	0.506	0.403	0.436	0.908	0.942	0.919
Angle	-	7	0.542	0.495	0.488	0.894	0.912	0.898
Angle	Smoothing	7	0.515	0.472	0.479	0.905	0.920	0.902
Angle	1st derivative	7	0.511	0.462	0.500	0.906	0.923	0.893
Angle	2nd derivative	5	0.571	0.529	0.488	0.883	0.899	0.898
Angle	SNV	8	0.480	0.438	0.497	0.917	0.931	0.895
Angle	SNV-Smoothing	8	0.490	0.447	0.506	0.914	0.928	0.891
Angle	SNV-1st derivative	7	0.452	0.416	0.482	0.927	0.938	0.901
Angle	SNV-2nd derivative	4	0.557	0.550	0.455	0.888	0.891	0.912
Height+Angle	-	8	0.512	0.449	0.516	0.906	0.928	0.886
Height+Angle	Smoothing	7	0.546	0.448	0.497	0.893	0.928	0.895
Height+Angle	1st derivative	7	0.520	0.492	0.497	0.903	0.913	0.895
Height+Angle	2nd derivative	4	0.632	0.595	0.528	0.856	0.872	0.881

Height+Angle	SNV	7	0.585	0.567	0.577	0.877	0.884	0.858
Height+Angle	SNV-Smoothing	8	0.495	0.451	0.556	0.912	0.927	0.868
Height+Angle	SNV-1st derivative	7	0.466	0.433	0.494	0.922	0.932	0.896
Height+Angle	SNV-2nd derivative	3	0.611	0.575	0.497	0.866	0.881	0.895

4.3.3. 3D Sugar content model of the whole surface of strawberry flesh

The PLSR results showed that all models had good prediction accuracy with R^2p greater than 0.85, so mapping was performed using the model with smoothing after height correction, which had the clearest map score in Chapter 4. Figure. 4-5 shows a 3D model visualizing the distribution of sugar content in the strawberry flesh part. The mapping results provide the distribution of sugar content in the flesh part of the entire fruit surface.

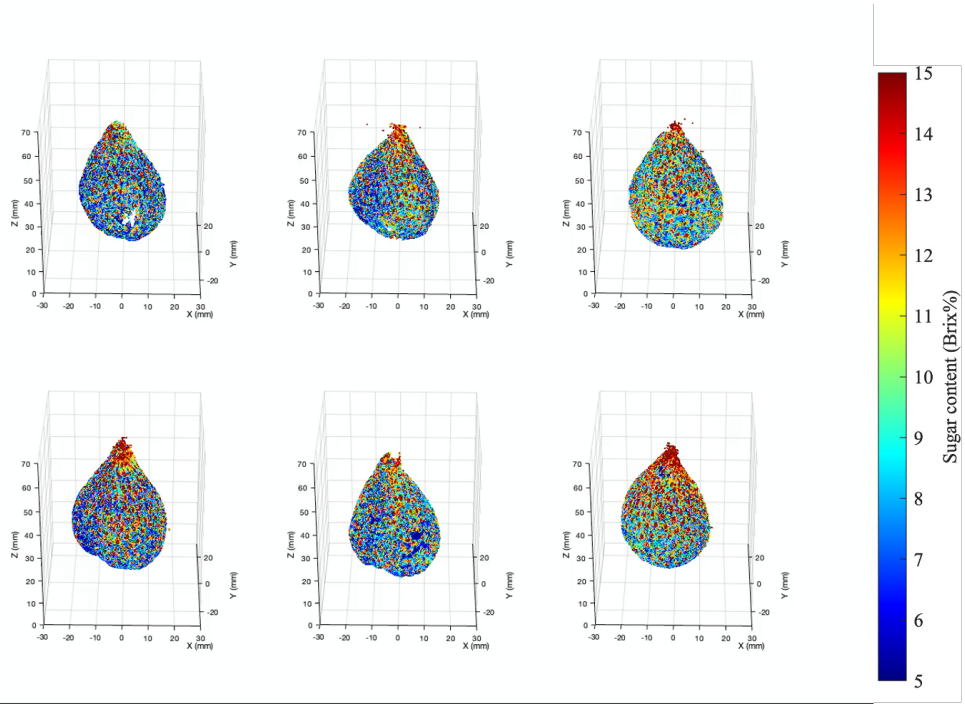

Figure 4-5. 3D Sugar content model of the whole surface of strawberry flesh. Samples are arranged from the upper left to the lower right so that the sugar content of the sample is higher from the upper left to the lower right.

4.4. Conclusion

Chapter 4 detailed the construction of a system capable of acquiring comprehensive spectral and shape information of a fruit, facilitated by the combined use of rotational line scan measurements and a turntable. This setup was employed to elucidate the distribution of sugar content within the flesh of an entire strawberry. The sugar content imaging using Hyperspectral data and shape data, acquired from a single complete rotation of the strawberry, were synthesized in a three-dimensional model to determine the fruit's shape and display the distribution of sugar content on the flesh of the fruit surface. The resultant 3D model represents a pioneering outcome in the field, providing the first depiction of sugar content distribution in the flesh of an entire strawberry.

5. Overview

The purpose of this paper was to overcome the problems in the NIR-HSI quality evaluation of strawberries and to establish a new quality evaluation method. The following results were achieved.

Ⅰ. a Near-Infrared NIR-HSI technique was employed to delineate the sugar content distribution within the flesh of white strawberries. Principally, PCA imaging distinguished the flesh from the remainder of the fruit, subsequently facilitating an evaluation of the sugar content distribution within the flesh alone via imaging and violin plots.

Ⅱ. The study further developed a three-dimensional imaging technique of the strawberry's sugar content, merging NIR-HSI with shape measurements. This process necessitated the examination of correction effects brought about by adjusting Hyperspectral data by factors of height and angle. A novel method was proposed for evaluating NIR-HSI mapping results, achieved by displaying the spatial distribution of sugar content in a three-dimensional context.

Ⅲ. The method was devised to measure HS data across the entire circumference of a strawberry using rotational scanning, subsequently allowing for the visualization of sugar content distribution in the flesh area within a 3D model.

The remaining challenges encompass the need to revisit the shape correction technique; the current situation fails to account for factors such as wavelength characteristics, and an optimal correction technique remains elusive. A reevaluation of the correction method via reference materials and shape samples is imperative. Likewise, the evaluation approach of mapping results calls for enhancement, specifically, an improvement in Mapscore to facilitate the judgment of noisy images. Other areas of investigation include practical application strategies for sorting, breeding, and variety improvement. This venture will necessitate consideration of measurement velocity and data resolution. Ultimately, an overarching quality evaluation, including shape and internal quality parameters (sugar content, acidity, sugar-acid ratio, and damage), is earmarked as a future undertaking.

Acknowledgment

I express acknowledgement to Associate professor Tetsuya Inagaki, Professor Satoru Tsuchikawa, Professor Kazuhiko Fukushima, Professor Hiromi Tokuda and Ma Te Project Assistant Professor in Nagoya University, colleagues in the laboratory and all faculties in Nagoya University for great support and educations, Colleagues in NARO, friends and family for great support.

References

Amodio, M.L., Ceglie, F., Chaudhry, M.M.A., Piazzolla, F., Colelli, G., 2017. Potential of NIR spectroscopy for predicting internal quality and discriminating among strawberry fruits from different production systems. Postharvest Biology and Technology 125, 112–121. https://doi.org/10.1016/j.postharvbio.2016.11.013

Andersson, M., 2009. A comparison of nine PLS1 algorithms. Journal of Chemometrics 23, 518–529. https://doi.org/10.1002/cem.1248

da Silva, F.L., Escribano-Bailón, M.T., Pérez Alonso, J.J., Rivas-Gonzalo, J.C., Santos-Buelga, C., 2007. Anthocyanin pigments in strawberry. LWT - Food Science and Technology 40, 374–382. https://doi.org/10.1016/j.lwt.2005.09.018

Darbellay, C., Carlen, C., Azodanlou, R., Villettaz, J.C., 2002. MEASUREMENT OF THE ORGANOLEPTIC QUALITY OF STRAWBERRIES. Acta Hortic. 819–822. https://doi.org/10.17660/ActaHortic.2002.567.181

ElMasry, G., Wang, N., ElSayed, A., Ngadi, M., 2007. Hyperspectral imaging for nondestructive determination of some quality attributes for strawberry. Journal of Food Engineering 81, 98–107. https://doi.org/10.1016/j.jfoodeng.2006.10.016

Fait, A., Hanhineva, K., Beleggia, R., Dai, N., Rogachev, I., Nikiforova, V.J., Fernie, A.R., Aharoni, A., 2008. Reconfiguration of the Achene and Receptacle Metabolic Networks during Strawberry Fruit Development. Plant Physiology 148, 730–750. https://doi.org/10.1104/pp.108.120691

Golic, M., Walsh, K., Lawson, P., 2003. Short-Wavelength Near-Infrared Spectra of Sucrose, Glucose, and Fructose with Respect to Sugar Concentration and Temperature. Appl Spectrosc 57, 139–145. https://doi.org/10.1366/000370203321535033

He, J.Q., Harrison, R.J., Li, B., 2017. A novel 3D imaging system for strawberry phenotyping. Plant Methods 13, 93. https://doi.org/10.1186/s13007-017-0243-x

Ikegaya, A., Toyoizumi, T., Ohba, S., Nakajima, T., Kawata, T., Ito, S., Arai, E., 2019. Effects of distribution of sugars and organic acids on the taste of strawberries. Food Science & Nutrition 7, 2419–2426. https://doi.org/10.1002/fsn3.1109

Kobori, H., Gorretta, N., Rabatel, G., Bellon-Maurel, V., Chaix, G., Roger, J.-M., Tsuchikawa, S., 2013. Applicability of Vis-NIR hyperspectral imaging for monitoring wood moisture content (MC). Holzforschung 67, 307–314. https://doi.org/10.1515/hf-2012-0054

Li, H.-D., Xu, Q.-S., Liang, Y.-Z., 2018. libPLS: An integrated library for partial least squares regression and linear discriminant analysis. Chemometrics and Intelligent Laboratory Systems 176, 34–43. https://doi.org/10.1016/j.chemolab.2018.03.003

Li, X., Wei, Y., Xu, J., Feng, X., Wu, F., Zhou, R., Jin, J., Xu, K., Yu, X., He, Y., 2018. SSC and pH for sweet assessment and maturity classification of harvested cherry fruit based on NIR hyperspectral imaging technology. Postharvest Biology and Technology 143, 112–118. https://doi.org/10.1016/j.postharvbio.2018.05.003

Lin, Y., Jiang, L., Chen, Q., Li, Y., Zhang, Yunting, Luo, Y., Zhang, Yong, Sun, B., Wang, X., Tang, H., 2018. Comparative Transcriptome Profiling Analysis of Red- and White-Fleshed Strawberry (Fragaria×ananassa) Provides New Insight into the Regulation of the Anthocyanin Pathway. Plant and Cell Physiology 59, 1844–1859. https://doi.org/10.1093/pcp/pcy098

Liu, Q., Sun, K., Peng, J., Xing, M., Pan, L., Tu, K., 2018. Identification of Bruise and Fungi Contamination in Strawberries Using Hyperspectral Imaging Technology and Multivariate Analysis. Food Anal. Methods 11, 1518–1527. https://doi.org/10.1007/s12161-017-1136-3

Liu, Q., Wei, K., Xiao, H., Tu, S., Sun, K., Sun, Y., Pan, L., Tu, K., 2019. Near-Infrared Hyperspectral Imaging Rapidly Detects the Decay of Postharvest Strawberry Based on Water-Soluble Sugar Analysis. Food Anal. Methods 12, 936–946. https://doi.org/10.1007/s12161-018-01430-2

Ma, T., Li, X., Inagaki, T., Yang, H., Tsuchikawa, S., 2018. Noncontact evaluation of soluble solids content in apples by near-infrared hyperspectral imaging. Journal of Food Engineering 224, 53–61. https://doi.org/10.1016/j.jfoodeng.2017.12.028

Magwaza, L.S., Opara, U.L., 2015. Analytical methods for determination of sugars and sweetness of horticultural products—A review. Scientia Horticulturae 184, 179–192. https://doi.org/10.1016/j.scienta.2015.01.001

Mizuki Tsuta, *, Junichi Sugiyama, † and, Sagara‡, Y., 2001. Near-Infrared Imaging Spectroscopy Based on Sugar Absorption Band for Melons [WWW Document]. ACS Publications. https://doi.org/10.1021/jf010854i

Mo, C., Kim, M.S., Kim, G., Lim, J., Delwiche, S.R., Chao, K., Lee, H., Cho, B.-K., 2017. Spatial assessment of soluble solid contents on apple slices using hyperspectral imaging. Biosystems Engineering 159, 10–21. https://doi.org/10.1016/j.biosystemseng.2017.03.015

Muñoz, C., Hoffmann, T., Escobar, N.M., Ludemann, F., Botella, M.A., Valpuesta, V., Schwab, W., 2010. The Strawberry Fruit Fra a Allergen Functions in Flavonoid Biosynthesis. Molecular Plant 3, 113–124. https://doi.org/10.1093/mp/ssp087

Otsu, N., 1979. A Threshold Selection Method from Gray-Level Histograms. IEEE Transactions on Systems, Man, and Cybernetics 9, 62–66. https://doi.org/10.1109/TSMC.1979.4310076

Pathmanaban, P., Gnanavel, B.K., Anandan, S.S., 2019. Recent application of imaging techniques for fruit quality assessment. Trends in Food Science & Technology 94, 32–42. https://doi.org/10.1016/j.tifs.2019.10.004

Pu, Y.-Y., Sun, D.-W., Riccioli, C., Buccheri, M., Grassi, M., Cattaneo, T.M.P., Gowen, A., 2018. Calibration Transfer from Micro NIR Spectrometer to Hyperspectral Imaging: a Case Study on Predicting Soluble Solids Content of Bananito Fruit (Musa acuminata). Food Anal. Methods 11, 1021–1033. https://doi.org/10.1007/s12161-017-1055-3

Salvatierra, A., Pimentel, P., Moya-León, M.A., Herrera, R., 2013. Increased accumulation of anthocyanins in Fragaria chiloensis fruits by transient suppression of FcMYB1 gene. Phytochemistry 90, 25–36. https://doi.org/10.1016/j.phytochem.2013.02.016

Sánchez, M.-T., De la Haba, M.J., Benítez-López, M., Fernández-Novales, J., Garrido-Varo, A., Pérez-Marín, D., 2012. Non-destructive characterization and quality control of intact strawberries based on NIR spectral data. Journal of Food Engineering 110, 102–108. https://doi.org/10.1016/j.jfoodeng.2011.12.003

Shrestha, B.P., Nagata, M., Cao, Q., 2001. Study on Image Processing for Quality Estimation of Strawberries (Part 1). Shokubutsu Kojo Gakkaishi 13, 115–122. https://doi.org/10.2525/jshita.13.115

Siedliska, A., Baranowski, P., Zubik, M., Mazurek, W., Sosnowska, B., 2018. Detection of fungal infections in strawberry fruit by VNIR/SWIR hyperspectral imaging. Postharvest Biology and Technology 139, 115–126. https://doi.org/10.1016/j.postharvbio.2018.01.018

Sturm, K., Koron, D., Stampar, F., 2003. The composition of fruit of different strawberry varieties depending on maturity stage. Food Chemistry 83, 417–422. https://doi.org/10.1016/S0308-8146(03)00124-9

Sun, M., Zhang, D., Liu, L., Wang, Z., 2017. How to predict the sugariness and hardness of melons: A near-infrared hyperspectral imaging method. Food Chemistry 218, 413–421. https://doi.org/10.1016/j.foodchem.2016.09.023

Tsurumi, R., Nakanishi, tatsuro, Yoshiyuki Ishihara, Ohashi, T., Kojima, N., Saitou, Y., Kobayashi, Y., Hatakeyama, A., Iimura, K., Handa, T., 2020. Breeding of a New Strawberry Cultivar with White Fruits “Tochigi i W1 go.” Bulletin of the Tochigi Prefectural Agricultural Experiment Station 81, 67–82.

Walsh, K.B., Blasco, J., Zude-Sasse, M., Sun, X., 2020. Visible-Nir 'Point' Spectroscopy in Postharvest Fruit and Vegetable Assessment: The Science Behind Three Decades of Commercial Use. Postharvest Biology and Technology 168, 111246. https://doi.org/10.1016/j.postharvbio.2020.111246

Weng, S., Yu, S., Dong, R., Pan, F., Liang, D., 2020a. Nondestructive detection of storage time of strawberries using visible/near-infrared hyperspectral imaging. International Journal of Food Properties 23, 269–281. https://doi.org/10.1080/10942912.2020.1716793

Weng, S., Yu, S., Guo, B., Tang, P., Liang, D., 2020b. Non-Destructive Detection of Strawberry Quality Using Multi-Features of Hyperspectral Imaging and Multivariate Methods. Sensors 20, 3074. https://doi.org/10.3390/s20113074

Włodarska, K., Szulc, J., Khmelinskii, I., Sikorska, E., 2019. Non-destructive determination of strawberry fruit and juice quality parameters using ultraviolet, visible, and near-infrared spectroscopy. Journal of the Science of Food and Agriculture 99, 5953–5961. https://doi.org/10.1002/jsfa.9870

Xiaona, L., Ruolan, L., Mengyu, W., Yaru, L., Baohua, Z., Jun, Z., 2018. Hyperspectral Imaging and Their Applications in the Nondestructive Quality Assessment of Fruits and Vegetables | IntechOpen. Hyperspectral Imaging in Agriculture, Food and Environment. InTech. https://doi.org/10.5772/intechopen.72250.

zhang, C., Guo, C., Liu, F., Kong, W., He, Y., Lou, B., 2016. Hyperspectral imaging analysis for ripeness evaluation of strawberry with support vector machine. Journal of Food Engineering 179, 11–18. https://doi.org/10.1016/j.jfoodeng.2016.01.002

Zhu, H., Chu, B., Fan, Y., Tao, X., Yin, W., He, Y., 2017. Hyperspectral Imaging for Predicting the Internal Quality of Kiwifruits Based on Variable Selection Algorithms and Chemometric Models. Sci Rep 7, 7845. https://doi.org/10.1038/s41598-017-08509-6